ELSEVIER

Contents lists available at ScienceDirect

Results in Engineering

journal homepage: www.sciencedirect.com/journal/results-in-engineering



Research paper

A study of the response dynamics of a Helmholtz resonator and its application in acoustic energy harvesting



- a School of Engineering, University of Derby, Derby, United Kingdom
- ^b School of Computing, University of Derby, Derby, United Kingdom
- ^c Department of Physics, Olabisi Onabanjo University, Ago-Iwoye, Ogun State, Nigeria

ARTICLE INFO

Keywords: Resonance Helmholtz resonator Piezoelectric Energy harvester Acoustics

ABSTRACT

A thorough understanding of the behaviour of Helmholtz resonators is required for their application in noise attenuation and energy harvesting systems. This paper proposes an efficient low-frequency acoustic energy harvester (AEH) designed as a Helmholtz resonator (HR) integrated with a piezoelectric film. A straightforward continuity equation that describes the compression of air molecules in the HR's cavity was used to represent the restoring force, thus allowing us to describe the dynamics of the air molecules as a classical particle of the Duffing-type oscillator. The variation of the resonant frequency of the HR device, with its geometry, was studied, which facilitated the investigation of the response dynamics of the system, using numerical, analytical, and experimental methods. It was demonstrated that an acoustically-driven HR can also exhibit jump or hysteresis behaviour at higher acoustic pressure. The system amplifies the sound pressure within the cavity, enhancing the vibration of the piezoelectric film, thereby improving the efficiency of the energy harvesting system. A significant amount of energy was generated with the HR, about four times the value obtained without the resonator. At resonance, the acoustic energy harvester generated a maximum voltage of 84.2 mV under a sound pressure level of 95 dB. The results confirm the capability, efficiency, and potential of the acoustic energy harvester as a sustainable energy solution for powering low-voltage devices in various applications.

1. Introduction

Ambient energies, such as vibration, heat, sound, etc., are ubiquitous. These environmental energies are generated from various sources, especially engineering structures. Such engineering structures include automobiles, trains, aircraft, wind turbines, industrial equipment, etc. High-speed movement, particularly when it involves vibrations or impacts, can generate acoustic energy, which can be converted into other useful forms of energy. The drive to reduce carbon emissions from fossil fuels has led to rapid development in the energy sector. This has motivated researchers to explore effective ways to convert ambient energies into useful electric energy. Several energy harvesting technologies have been explored to minimize the dependency on fossil fuel and support the use of energy in homes, industries, automobiles, and information technology [1].

Ambient vibration energy can be harvested in the form of electrical energy, which can be used to power low-voltage devices, in electric

vehicles, rail infrastructures and rolling stocks, roadside and rail-side lighting systems, on-board electronics, etc. Wind turbines are the oldest known method of harnessing airflow energy. Due to bearing losses and very significant viscous drag on the blades, at low Reynolds numbers, the performance of a small-scale wind turbine system is average, while large-scale wind turbine systems can be quite efficient [1-3]. Meanwhile, bearing-free devices are a superior option for small-scale applications. Several airflow energy harvesters, utilizing mechanical vibration, have been developed in recent years [2]. There are two major technological advancements in this regard; the first form uses the drag force generated by the air flow, while the second form converts air motion into steady oscillations of air molecules [4]. Usually, in the first form, a piezoelectric or magnetoelectric structure vibrates, as a result of the airflow's drag force, thereby converting the kinetic energy, due to the structure's motion, into electrical energy. However, in the second form, a Helmholtz resonator (HR) is used to convert the airflow motion into stable oscillations of the air molecules. The piezoelectric

E-mail address: U.Diala@derby.ac.uk (U.H. Diala).

https://doi.org/10.1016/j.rineng.2025.106470

Received 4 May 2025; Received in revised form 4 July 2025; Accepted 23 July 2025

^{*} Corresponding author.

| Glossary of nomenclature and abbreviations | | | | | | | | | |
|---|--|--------------------|--|--|--|--|--|--|--|
| Roman letters A_c Amplitude of the cosine component | | | Volume of resonator's cavity | | | | | | |
| A_c AEH | Acoustic energy harvester | $V_{oc} \ V_{RMS}$ | Root-mean-square voltage Volt | | | | | | |
| | Linearized response amplitude of the output signal | x(t) | Dimensionless displacement of air molecule | | | | | | |
| A_L AMMs | Acoustic metamaterials | \ddot{x} | Second derivative of $x(t)$ w.r.t time | | | | | | |
| A_n | Area of resonator's neck | y(t) | Instantaneous displacement of air in cavity | | | | | | |
| A_p | Amplification factor for sound pressure | Greek letters | | | | | | | |
| A_{s} | Amplitude of the sine component | | | | | | | | |
| A_r | Amplitude of displacement | α | Coefficient of quadratic stiffness nonlinearity | | | | | | |
| c | Speed of light m/s | β | Coefficient of cubic stiffness nonlinearity | | | | | | |
| d | Distance from sound source to AEH | γ | Specific heat ratio of air | | | | | | |
| F | Amplitude of sound wave | δ | The linear damping term | | | | | | |
| F_c | Critical pressure amplitude | ϵ | Quantifier of response amplitude, Q | | | | | | |
| f f | Frequency of sound wave Hz | η | Logarithmic power sensitivity dB | | | | | | |
| | Natural frequency of piezoelectric material | θ | Phase angle | | | | | | |
| f_n | Helmholtz number | κ | Sensitivity of open-circuit voltage | | | | | | |
| H_e HR | Helmholtz rumber Helmholtz resonator | $\lambda_{1,2}$ | Coefficients of least squares linear fit equation | | | | | | |
| | | μ | Sum of acoustic and friction impedance Ns/m ⁵ | | | | | | |
| I_p | Induced current | ξ | Output power per unit area µW/m ² | | | | | | |
| L | Length of cantilever beam | ρ | Density of the air kg/m ³ | | | | | | |
| L_n | Length of the HR's neck | $\sigma_{1,2}$ | Coefficients of rescaled linear fit equation | | | | | | |
| L_{eff} | Effective length of the HR's neck | au | Times | | | | | | |
| n | Number of complete oscillations | τ_p | Coupling factor of between charge and voltage | | | | | | |
| ODE | Ordinary Differential Equation | $\dot{\phi}$ | Empirical scaling factor | | | | | | |
| P | External acoustic pressure | χ | Piezoelectric displacement | | | | | | |
| p_{atm} | Atmospheric pressure N/m ² | ω | Frequency of acoustic excitation Hz | | | | | | |
| P_e | Electrical power extracted | ω_0 | Linear resonant frequency of HR Hz | | | | | | |
| $P_{e_{in}}$ | Input acoustic power | ω_{rex} | Experimental resonant frequency Hz | | | | | | |
| $P_{e_{out}}^{"}$ | Output electrical power | Ω | Unit of resistance | | | | | | |
| p_{in} | Input acoustic pressure | Ω_f | Dimensionless frequency | | | | | | |
| p_{out} | Output acoustic pressure | Ω_{max} | Resonant frequency at maximum response | | | | | | |
| PVDF | Polyvinylidene Fluoride | Ω_n | Dimensionless natural resonant frequency | | | | | | |
| Q | Response amplitude | Ω_{ran} | Dimensionless ω_0 | | | | | | |
| Q_{ana} | Analytical response amplitude | Ω_{rex} | Dimensionless ω_{rex} | | | | | | |
| Q_{num} | Numerical response amplitude | | · | | | | | | |
| R_L | Load resistance | Symbols | | | | | | | |
| R_{opt} | Optimal resistance | $\Delta \psi$ | Change in ψ | | | | | | |
| SPL | Sound pressure level | $ \psi $ | Absolute value of ψ | | | | | | |
| t | Dimensionless time | overdot | Time derivative | | | | | | |
| T | Period of oscillations | $\sqrt{\psi}$ | Square roof of ψ | | | | | | |

strip is strategically positioned at the base of the resonator, where the vibration of the air molecules within the HR chamber causes it to oscillate. The Helmholtz resonator and the piezoelectric strip used should have approximately the same resonant frequency, allowing both devices to resonate concurrently, which ensures a general optimal performance [5]. Most energy harvesting systems perform poorly due to a frequency mismatch between the resonant frequency of the generator and ambient vibrations [6-8]. In addition, most energy harvesters are designed to harvest energy within a narrow bandwidth, thus limiting their ability to harvest ambient vibrations that have frequencies beyond their operational bandwidth. For example, a three-degree-of-freedom acoustic energy harvester was developed by Izhar and Khan [9], using a piezoelectric plate with a circular block and a cantilever beam coupled with a Helmholtz resonator. The device was developed to add degree of flexibility, such as a cantilever beam, to the narrow frequency spectrum of traditional acoustic energy harvesters. Their results showed that the harvester can have three resonant peaks. Therefore, energy harvesting systems must be designed to accommodate a wide band of vibration frequencies, as encountered in many applications [6,8,10].

A Helmholtz resonator is a very classic acoustic system that has been extensively studied [11–15]. With the thriving development of meta-

material technologies in recent years and their applications in energy harvesting, Helmholtz resonators have found widespread use in the fabrication of acoustic energy harvesters and acoustic metamaterials for sound enhancement and noise reduction, respectively [16-20]. In other words, metamaterials are specially designed materials, engineered to enhance mechanical, acoustic, electrical, or optical processes [21,22]. Acoustic metamaterials (AMMs) are manufactured specifically to control, direct, and manipulate sound waves, enabling applications such as sound absorption [16,23], amplification, acoustic cloaking [24,25], sound focusing [26,27], and perfect absorption [28,29]. These systems often utilize Helmholtz resonators, which enhance sound pressure in specific frequency bands and attenuate others [30–32]. Hence, the need to investigate the dynamic response of HR devices cannot be overemphasized. For example, knowledge of the nonlinear behaviours of HR devices has led to significant progress in modern acoustic engineering, and has been applied in the development of nonlinear acoustic superlenses [33,34], acoustic diodes [35,36], photonics metamaterials [37], and acoustic switching and rectification [38].

Recently, researchers have attempted to improve the efficiency of vibration energy harvesters (VEHs), particularly for broadband energy harvesting. Several nonlinear oscillator models have been proposed to

study the dynamic response of VEHs [39–43]. However, in acoustic energy harvesting, the HR cavity facilitates the sound amplification capability of the AEH, with a possible dual-function mode (noise reduction and energy generation) [44]. This shows its potential to simultaneously achieve energy harvesting and noise attenuation. This concept offers prospects for the implementation of sustainable energy generation, which is useful for low-power devices, such as wireless sensor networks (WSNs), a significant component of the Internet of Things (IoT) [5,7,45]. Furthermore, piezoelectric materials offer the benefit of instant energy generation from impact, with a high transduction efficiency, which justifies their widespread applications and the growing interest of researchers [7,46].

The performance of the AEH in harvesting sound energy has been achieved by focusing on enhancing the cavity of the HR unit. For example, due to the low intensity of the sound from acoustic sources, Yuan et al. [47] suggested improving the output power of an acoustic energy harvester and presented a unique method for its implementation. The core component of the proposed high-performance system was an HR unit with an adjustable base, suitable for low-frequency sound waves [47]. An autonomous micro-electromechanical system (MEMS) built on an AEH with an HR unit, by Horowitz et al. [48], provided evidence for the viability of acoustic energy harvesting. Liu et al. [49] revealed that a piezoelectric patch and an HR unit can be coupled together to provide a maximum power of about 30 mW, when excited to 161 dB Sound Pressure Level (SPL). Under a sound pressure excitation of about 960 Hz tone and SPL of 100 dB, a proposed dual Helmholtz resonator structure, with increased acousto-electric coupling, produced a maximum power of 1.3 mW [50]. Similarly, the same authors further suggested a wide-band AEH prototype design, which was tested and reported to be more efficient [51]. Furthermore, the mass of air that flows through the aperture (neck) of an HR device inspired Kim et al. [52] to build an acoustic energy harvester that uses large-amplitude acoustic waves. A piezoelectric cantilever integrated with a Helmholtz resonator was proposed by Noh et al. [53], where the mechanical resonance of the cantilever aligned with the acoustic resonance of the HR device, to optimise the efficiency of the energy harvesting system.

Wang et al. [44] presented a unique renewable acoustic energy harvester and noise barrier design that uses a Polyvinylidene Fluoride (PVF) film and an HR unit. They reported that a unit of the system could generate a maximum instantaneous output voltage of about 74.6 mV at 110 dB (SPL) [44]. Li et al. [54] developed a tunable low-frequency acoustic energy harvester designed to convert the sound energy in a subway tunnel into electrical energy. Their experimental results showed the possibility of generating an instantaneous 317.5 mV, and a maximum instantaneous power of about 100.8 µW, at 100 dB, demonstrating the feasibility and effectiveness of dual-function noise barrier and sound energy harvesting systems. A high-density acoustic energy harvester was designed with metamaterial and Helmholtz coupled resonator (MHCR) in [55]. The MHCR unit was introduced to enhance the sound energy density. They reported a maximum transmission ratio of 30.83 mV/Pa, and the maximum voltage of the coupled energy harvester was approximately 3.5 times that of the maximum voltage of the metamaterial energy harvester. In other studies, resonance coupling strategies have been reported to be an effective way to improve the extracted sound energy [8,50,56]. For example, the coupled acoustic crystal designed by [57] has an efficiency higher than that of a single HR.

Most recently, a piezoelectric self-powered system, anchored on a Conical-Neck Helmholtz Resonator-Based Piezoelectric Self-Powered System (CNHR-PSS), was designed in [58] The system included a Piezoelectric Self-Powered Node (PSN) and a machine learning algorithm. The PSN, employing the Conical Neck Helmholtz Resonator and piezoelectric module, captures noise and transmutes it into electrical energy, while the multiple PSNs connect to form a sound barrier for traffic noise mitigation. Their experimental results showed the possibility of generating an output power of approximately 0.52 mW, and an average noise reduction of 13.16%. One of the most recent innovative designs

of an acoustic energy harvesting device was made by Li et al. [59]. It is based on the topological arrangement of multi-resonant phononic crystals, where the introduction of multiple resonant cavities reduced the operating frequency and improved robustness. Zhang et al. [18] developed a multi-tube parallel Helmholtz resonator-based triboelectric nanogenerator (MH-TENG) to harvest sound energy in low-frequency noise situations. The MH-TENG is made up of a thin-film transducer and a modified HR. Their experimental results showed an enhanced power generation due to the improved design of the sound wave collector within a narrow bandwidth.

A combination of the HR device and a piezoelectric sensor, in the form of a cantilever beam structure, has been subjected to similar investigations [60,61]. Note that unless active/semi-active control methods are applied, characteristic low-frequency noise with a comparatively long wavelength has a higher endurance capability. Hence, when it comes to the applications of AEH, low-frequency sound waves are a more prevalent ambient energy source than sound waves in the mid/high frequency range. Since the amount of energy harvested, using a piezoelectric strip in AEHs, depends on the resonant frequency of the host HR device, it is important to fully understand the dynamics of the host system (in this case the HR unit). Generally, a properly designed acoustic resonator is required to ensure that the acoustic energy harvester adequately amplifies the incident acoustic pressure and generates a large pressure difference. This is to facilitate effective lowfrequency sound wave conversion to electricity using the piezoelectric element. However, the complex behaviour of the HR unit, which arises mainly from several types of dissipation forces, can limit its effect on AEH designs or restrict installation processes.

Recent studies in HR devices focus on nonlinear damping and restoring forces to enhance the dynamic behaviour and efficiency of the unit. Singh and Rienstra [13] modelled the HR unit using a linear restoring force and a nonlinear damping element, identifying vortex shedding as a key cause of nonlinear dissipation, while thermo-viscous boundary layers contributed to linear dissipation. Förner et al. [14] highlighted the influence of neck geometry on vortex dissipation and dynamic behaviour. Nonlinear damping from jet loss and nonlinear restoring forces, due to cavity air elasticity at large amplitudes, were studied by Alamo Vargas et al. [30] and Vakakis [62], with Vakakis [62] reporting softening behaviour. Meissner [11] confirmed the dependence of HR frequency on flow characteristics and resonator shape. To minimize vortex dissipation while investigating nonlinear dynamics, Alamo Vargas et al. [30] modified the neck geometry, achieving both softening and hardening behaviours and enabling the calculation of extreme nonlinear responses in HR systems. Most recently, Omoteso et al. [31] investigated the motion of air particles in an HR cavity under sound wave excitation, focusing on vibrational resonance (VR) phenomena. The study examined the combined effects of amplitude and frequency on particle motion and resonance induction, highlighting nonlinear behaviours, including the attenuation of VR under specific conditions linked to excitation frequency and resonator geometry. The findings identified optimal performance regimes that enabled the design of broadband acoustic resonators for various applications.

While most existing studies rely on idealized models that overlook key structural features critical to improving practical Helmholtz resonator (HR) design, this paper introduces a simple yet effective approach to acoustic energy harvesting by integrating a Helmholtz resonator with a piezoelectric film. The system is modelled using a nonlinear Duffing-type oscillator derived from fundamental air compression principles, enabling it to capture complex dynamic behaviours, such as jump and hysteresis effects, that are often missed in conventional analyses. To investigate the resonance characteristics and optimise the design of a low-frequency HR for energy harvesting, Newton's laws were employed to model air motion through the neck and within the cavity using techniques reported in prior studies [30,31]. The system's response was then analysed using classical resonance methods to determine the fundamental resonant frequency relevant for acoustic energy harvest-

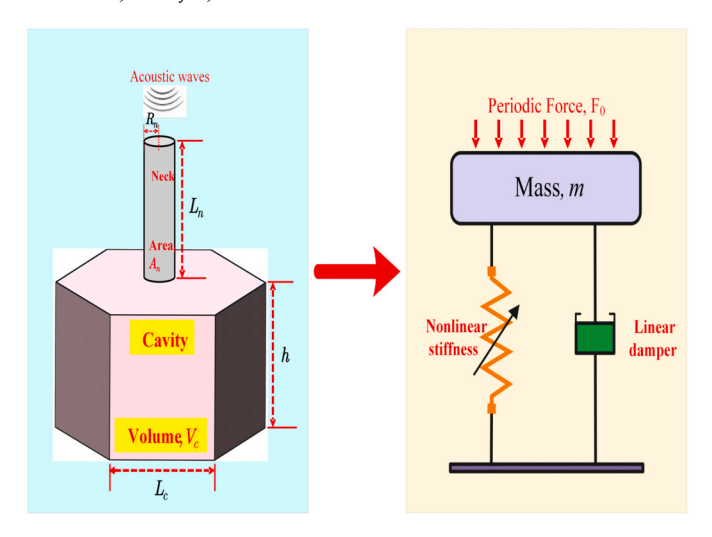


Fig. 1. The Helmholtz resonator modelled as a mass-spring-damper system with stiffness nonlinearity.

ing. Compared to setups without the resonator, the proposed design shows the potential to achieve a fourfold increase in harvested energy, demonstrating a strong possibility for powering low-power devices in real-world applications.

The rest of the paper is organized as follows: The description of the HR unit and the modelled nonlinear equation is given in the next section (Section 2). Section 3 discusses the resonance dynamics of the HR system, both analytically and numerically. The experimental setup and measurement procedures are presented in Section 4. Although Section 5 contains the results and discussions of our findings, the system performance metric and the average power generated by the AEH are estimated in its subsections. Lastly, a summary of the paper and some significant applications of our findings are provided in Section 6.

2. Model description

The model of interest in this research is the Helmholtz resonator, which presents a fascinating resonance behaviour, especially when the air in its chamber or cavity resonates. The Helmholtz resonator is an acoustic resonator that produces the highest sound pressure at the resonant frequency dictated by the chamber's volume and neck size. A Helmholtz resonator, which consists of a gas-filled chamber with an open neck, can be modelled as a mass-spring-damper system, as shown in Fig. 1. The mass represents the air volume in the neck, while the spring and damper represent the air volume in the cavity. To improve the performance of the acoustic energy harvesting device, the Helmholtz resonator is designed, with the appropriate structural dimensions, to ensure that its resonant frequency matches that of the coupled piezoelectric strip situated in the cavity. The acoustic resonator with a hexagonal prism chamber is constructed as an HR device to match the benefits of a honeycomb noise collection structure. The area and the volume of the resonator's cylindrical neck and hexagonal-shaped cavity, respectively, can be calculated from

$$A_n = \pi R_n^2 \text{ and}$$

$$V_c = \frac{3\sqrt{3}}{2} l_c^2 h$$
(1)

where R_n is the radius of the neck, h is the height of the hexagonal prism (the HR's cavity), and l_c is the regular hexagon side-length. The parameters of the HR unit are presented in Table 1. The sound pressure amplification factor, A_p of a Helmholtz resonator with a negligible wall loss at resonance is expressed as the ratio of the output acoustic pressure, p_{out} , in the cavity, to the input acoustic pressure, p_{in} , expressed as [44, 53]

Table 1Parameter values of the HR prototype.

| Description | Value (mm) |
|-----------------------------------|------------|
| Radius of neck, R_n | 5.0 |
| Length of neck, L_n | 42 |
| Height of hexagonal cavity, h_c | 65 |
| Side length of the hexagon, l_c | 55 |

$$A_{p} = \frac{p_{out}}{p_{in}} = 2\pi \sqrt{\frac{L_{n}^{3} V_{c}}{A_{n}^{3}}}.$$
 (2)

The pressure in the cavity, p_{out} is also a function of the HR resonant frequency, ω_0 , in the form [44]

$$p_{out} = A_p p_{in} = \frac{c p_{in}}{\omega_0} \left(\frac{L_n}{A_n} \right). \tag{3}$$

Equations (1) to (3) indicate that the resonant frequency and the sound amplification capacity of the system depend on the length of the neck (L_n) , and radius of the neck (R_n) , which defines the cross-sectional area (A_n) , and the volume of the cavity (V_c) . Moreover, the fundamental resonant frequency of the air vibration in response to the incident acoustic pressure across the opening can be expressed as

$$\omega_0 = \frac{c}{2\pi} \sqrt{\frac{A_n}{V_c L_{eff}}}.$$
(4)

Note that ω_0 is the linear resonant frequency of the Helmholtz resonator [44,47,53], where c is the speed of sound in air, A_n is the cross-sectional area of the oscillator's cylindrical neck, and V_c is the volume of the cavity or chamber. L_{eff} represents the effective length of the neck, accounting for both its actual length (L_n) and a correction (ΔL_n) for the additional inertial mass of air above the neck region. The effective neck length, L_{eff} , is influenced by whether its ends are flanged or unflanged, with $L_{eff} = L_n + 1.7R_n$ as the approximation for the fully flanged case [53].

The prototype was designed to facilitate noise collection and improve the performance of the HR unit for significant energy harvesting. Therefore, a noise collection section is incorporated into the Helmholtz resonator (HR) in the form of a funnel, and through the structure, the ambient acoustic wave is gathered and channeled into the HR's cavity via the neck. The neck connects the funnel to the Helmholtz resonator chamber, forming a passage for the air molecules that resonate in the HR's cavity. At resonance, frequency matching occurs, and under such conditions, the resonating system acquires a huge amount of energy [63]. The sound pressure is significantly amplified at resonance at a characteristic frequency (ω_0), in the HR cavity. Therefore, to simultaneously boost noise collection and improve energy harvesting, a hexagonal prism chamber is designed as the HR cavity. However, it is worth noting that the cavity of the HR device is responsible for the amplification of the resonant pressure and plays a vital role in defining the resonant frequency of the Helmholtz resonator structure. In addition, acoustic resonance produces the highest sound pressure when the incident acoustic frequency and the cavity's resonant frequency, which depends on the cavity volume and HR neck dimensions, are equal [44,53].

To study the resonance dynamics of the prototype described in Fig. 2, we utilise the HR parameters to derive a dimensionless displacement equation. The displacement y of air in the neck causes a change in pressure (ΔP) , which can be expressed as [30,31]

$$\Delta P = -\psi \left[y - \frac{(\gamma + 1)A_n}{2V_c} y^2 + \frac{(\gamma + 1)(\gamma + 2)A_n^2}{6V_c} y^3 \right],\tag{5}$$

where $\psi = \rho \omega_0^2 L_{eff}$ and ρ ($\rho = 1.29 \text{ kg/m}^3$) is the density of air. L_{eff} ($L_{eff} = 5.05 \times 10^{-3} \text{ m}$) and A_n ($A_n = 7.86 \times 10^{-5} \text{ m}^2$) are the effective length and the cross sectional area of the neck, respectively. V_c ($V_c = 5.00 \times 10^{-4} \text{ m}^3$) is the effective volume of the cavity, obtained

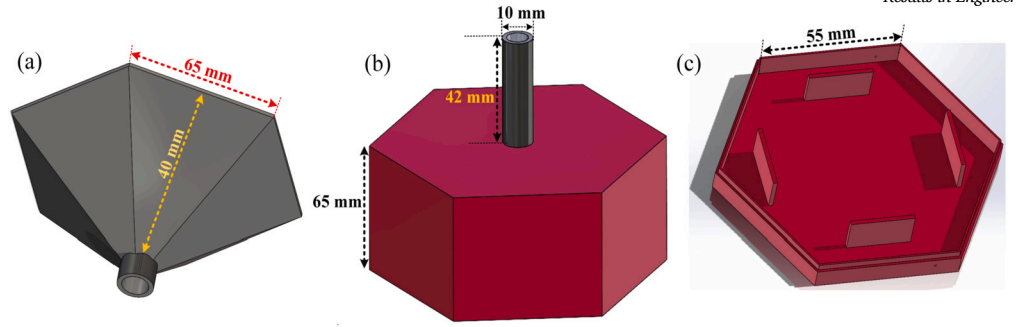


Fig. 2. CAD design of the HR prototype using the SOLIDWORKS software. (a) The dimension of the honeycomb sound collector, (b) the dimensions of the hexagonal shaped cavity and the cylindrical neck of the designed Helmholtz resonator, and (c) the dimension of the HR base, showing the provision for the attachment of multiple piezoelectric films.

by subtracting the volume of the four rectangular-stands, designed for the attachment of multiple piezoelectric strips, from that of the hexagonal prism. γ is the specific heat ratio of air. Thus, the equation of motion with respect to time τ (s), takes the form [30–32],

$$\frac{d^2y}{d\tau^2} + \left[\frac{\mu A_n}{\rho L_{eff}}\right] \frac{dy}{d\tau} + \omega_0^2 y - \left[\frac{\alpha A_n \omega_0^2}{V_c}\right] y^2 + \left[\frac{\beta A_n^2 \omega_0^2}{V_c^2}\right] y^3 = -\left[\frac{p_{atm}}{\rho L_{eff}}\right],$$
(6)

where μ (413 Ns/m⁵) [64], accounts for the sum of the acoustic and friction impedance at the inlet of the HR. $\alpha = \frac{(\gamma+1)}{2}$, $\beta = \frac{(\gamma+1)(\gamma+2)}{6}$, and p_{atm} (N/m²) is the pressure variation around atmospheric pressure.

Since air oscillation in the cavity is assumed to be a simple mass-spring model, typically the essential source of nonlinear restoring force in the system [13,14,32], the description of the nonlinear behaviour of our HR model is derived by only taking into account the nonlinearity of the restoring force of the spring, while the nonlinearity of damping is neglected. Moreover, it is important to note that the high velocity air in the HR's neck causes friction that results in damping, while the relative change in the pressure in the cavity due to displacement of the air in the neck induces a restoring force [32]. This can be written in nonlinear form with α and β representing the quadratic and cubic nonlinear coefficients, respectively. Additionally, the effect of varying these parameters (α and β), particularly the coefficient of cubic stiffness, β , on the potential structure and response dynamics of HR has been studied in [31].

The specific heat ratio of air, γ , which characterises the thermodynamic condition of the air molecules, determines the potential parameters, α and β . The gas's specific heat ratio (γ) is the ratio of its specific heats at constant pressure to that at constant volume. The type of the air molecules and the acoustic wave's excitation frequency determine the specific heat ratio of the air molecules in the neck. In general, adiabatic processes occur in the cavity due to an increasing temperature gradient if the driving frequency is excessively high. Otherwise, the process becomes isothermal at low driving frequencies [31]. Consequently, α and β are dependent on the specific heat ratio of air, γ . An intermediate value for the specific heat ratio, $\gamma=1.4$, can be utilised to define the thermodynamic condition of the air molecules in the cavity and across the neck [31]. The dimensionless nonlinear equation describing the motion of air molecules passing through the neck into the HR cavity, driven by an external acoustic pressure, p_{atm} , can be rewritten as

$$\ddot{x} + \delta \dot{x} + x - \alpha x^2 + \beta x^3 = P,\tag{7}$$

where ${\cal P}$ is the external acoustic excitation that determines the system's response behaviour. Other parameters of the system are rescaled using

$$t = \omega_0 \tau$$
, $x = \frac{A_n y}{V_c}$, $\delta = \frac{\mu A_n}{\rho \omega_0 L_{eff}}$, and

$$P = -\frac{A_n p_{atm}}{\rho V_c \omega_0^2 L_{eff}}.$$
(8)

In Eq. (7), δ , which represents linear damping coefficient, facilitates the description of the dynamics of the system. Usually, nonlinear damping can be ignored at low levels of sound pressure, but at high levels of sound pressure, it is proportional to the cavity-to-neck volume ratio and plays a significant role in the dynamic response of the system [13,32,62].

3. Resonance dynamics of the HR system

In this section, we describe the response dynamics of the HR model using system (7), with respect to the external acoustic excitation. It is important to note that the significant dynamic regimes of the HR model depend on its size and dimension. Hence, to study the resonance behaviour of the modelled nonlinear equation, system (7), we assume that the acoustic excitation, P, is composed of both the amplitude F and the frequency ω , of the sound wave. This is such that $|P| = F \cos \Omega_f t$, where $\Omega_f = \frac{\omega}{\omega_0}$, the dimensionless frequency. It is worth noting that the goal is to optimise the HR's response for efficient acoustic energy harvesting, and the underlying principle is that the wavelength of the acoustic wave, associated with the sound pressure oscillations, is much longer than the resonator's dimension. Hence, the pressure oscillation can be considered to have the same phase at every point within the resonator [53,65].

3.1. Analytical description

To provide strong and convincing points on the dynamic response of the HR model described by system (7), it is logical to treat the model as a typical mechanical oscillator for a simple analysis. Therefore, Eq. (7) can be rewritten as

$$\ddot{x} + \delta \dot{x} + \Omega_{n}^{2} x - \alpha x^{2} + \beta x^{3} = F \cos \Omega_{f} t, \tag{9}$$

where $\Omega_n^2 = 1$, the natural resonant frequency of system (7). In a linearized form, Eq. (9) becomes

$$\ddot{x} + \delta \dot{x} + \Omega_n^2 x = F \cos \Omega_f t, \tag{10}$$

which has a steady state solution of the form $x(t) = A_L \cos(\Omega_f t + \theta)$, and the response amplitude, A_L given by

$$A_{L} = \frac{F}{\sqrt{(\Omega_{n}^{2} - \Omega_{f}^{2})^{2} + (\delta\Omega_{f})^{2}}}$$

$$\theta = -\tan^{-1}\left(\frac{d\Omega_{f}}{(\Omega_{n}^{2} - \Omega_{f}^{2})}\right)$$
(11)

Therefore, the response amplitude, Q is

$$Q_{ana} = \frac{A_L}{F} = \frac{1}{\sqrt{\varepsilon}},\tag{12}$$

where $\varepsilon=\sqrt{(\Omega_n^2-\Omega_f^2)^2+\delta^2\Omega_f^2}$. The magnitude of F changes with variation in the amplitude of the external acoustic force. Hence, the instantaneous pressure of the acoustic field is proportional to the instantaneous displacement, x of the system. Moreover, the condition for Q to be maximum is $\frac{d\varepsilon}{d\Omega_f}=0$ and $\frac{d^2\varepsilon}{d\Omega_f^2}<0$. From these conditions, the value of Ω_f at which Q is maximum can be obtained from [63,65–67],

$$\Omega_{max} = \sqrt{\Omega_n^2 - \frac{\delta^2}{2}}. (13)$$

This shows the influence of the linear damping term, δ on the resonant frequency and the response amplitude Q of the HR system. However, for an infinitesimal value of δ , the maximum resonant frequency of the response amplitude, Eq. (12) is

$$\Omega_{max} = \sqrt{\Omega_n^2}. (14)$$

Evidently, $\Omega_{max} = \Omega_n$, the natural resonant frequency of the system, and is used for both analytical and numerical investigations in this study, except otherwise specified. This is because at the resonant frequency, even a small amplitude periodic driving force will be able to produce large amplitude oscillations.

3.2. Numerical simulations

To validate the analytically computed response amplitude Q, we numerically integrate the nonlinear HR oscillator (Eq. (9)) using the estimated parameter values. This is achieved by first calculating the linear resonant frequency of the system, ω_0 from Eq. (4). The frequency in the linear regime as defined by the equation (4) is $\omega_0 = 96.23$ Hz. Next, we rewrite Eq. (9) as a set of coupled first-order ordinary differential equations (ODE) of the form:

$$\frac{dx}{dt} = \dot{x}$$

$$\frac{d\dot{x}}{dt} = -\delta \dot{x} - \Omega_n^2 x + \alpha x^2 - \beta x^3 + F \cos \Omega_f t.$$
(15)

Eq. (15) was integrated using the Fourth-Order Runge-Kutta scheme with a fixed step size $\Delta t=0.001$, and the following parameters, calculated from Eq. (8), were fixed throughout the analysis; $\delta=0.0661, \Omega_n^2=1.0$, $\alpha=1.20$, $\beta=1.36$. We considered zero initial conditions, that is x(t)=0 and $\dot{x}(t)=0$, so that the output time series of Fourier sine and cosine components are Q_s and Q_c , respectively. Hence, the response amplitude, Q_s , is calculated from

$$Q_{num} = \frac{\sqrt{Q_s^2 + Q_c^2}}{F}$$

$$\theta = -\tan^{-1}\left(\frac{Q_s}{Q_c}\right),$$
(16)

where,

$$Q_{s} = \frac{2}{nT} \int_{0}^{nT} x(t) \sin \Omega_{f} t dt,$$

$$Q_{c} = \frac{2}{nT} \int_{0}^{nT} x(t) \cos \Omega_{f} t dt.$$
(17)

The period of oscillation is given as $T = \frac{2\pi}{\Omega_f}$, where n = [1, 2, 3, ...] is the number of complete oscillations. To validate the theoretical results

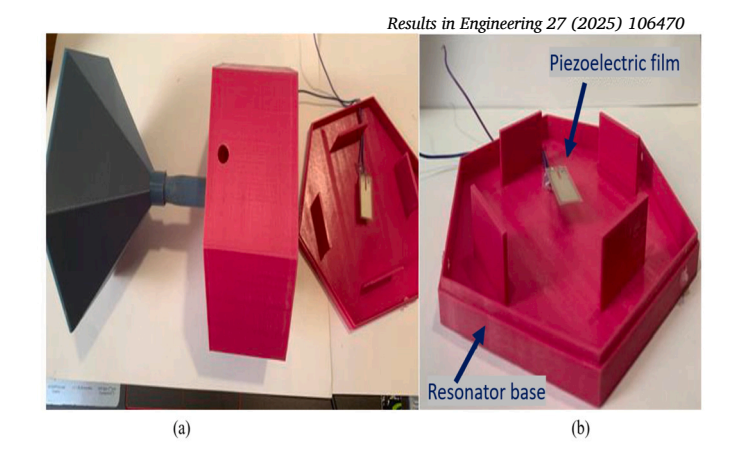


Fig. 3. (a) The uncoupled prototype HR design. (b) Bottom cover of the HR, showing the position of the piezoelectric film for acoustic energy harvesting.

in subsection 3.1, the analytically computed response amplitude, Q_{ana} obtained using Eq. (12), is compared with the results of the direct numerical integration, Eq. (16).

4. Experimental set-up and measurement procedures

The 3D-printed design of the Helmholtz resonator (HR) device is shown in Fig. 3. It was fabricated using polylactic acid (PLA), a thermoplastic polymer widely used in additive manufacturing (AM) due to its low cost, ease of processing, and dimensional stability, with features that make it suitable for a variety of engineering applications. Recent advances in AM have enabled the rapid prototyping of acoustic structures such as HRs using materials like PLA, offering cost-effective fabrication and geometric flexibility. However, the acoustic performance of AM-fabricated HRs can be affected by manufacturing-related factors such as surface roughness, internal porosity, and dimensional tolerance deviations [68-70]. These factors may lead to shifts in the resonance frequency or a broadening of the response bandwidth, potentially affecting the accuracy of acoustic energy harvesting systems. Despite these limitations, controlled AM processes have been shown to yield acoustically functional structures, as demonstrated in [71]. PLA remains a practical and valid material for prototyping, especially in early-stage acoustic or energy harvesting research, where parametric studies and iterative testing are essential.

Figs. 3a and 3b show the uncoupled resonator and the installed Polyvinylidene Fluoride (PVDF) film for energy harvesting, discussed in Section 5.2. Moreover, the sound pressure level measuring devices (SPL meters) and the sound wave generator (Audio minirator) are shown in Fig. 3c. The experimental setup is shown in Fig. 4. The experiment was conducted in an anechoic chamber to isolate the test rig from environmental noise and to eliminate reflected sound waves. This is done to ensure that only the incident sound pressure generated by the acoustic source is effectively received and amplified by the HR device. The experimental setup consists of the Helmholtz resonator prototype and a minirator (MR-PRO) connected to a loudspeaker (Genelec 8030C), providing a complete set of analogue audio signals (sine waves). In addition, a set of input and output acoustic waves, associated with the HR unit, are measured using two sensitive microphones, which are connected to their corresponding sound level meters (NTi-XL2). Useful pressure amplitude data are acquired for analysis and system optimisation. To ensure repeatability and reliability, all measurements were conducted multiple times under the same experimental conditions. Each data point in the presented plots represents the average of at least three independent trials. The analog oscilloscope (RTB-2004) is connected to display the generated voltage waveform of the acoustic energy harvester, when the piezoelectric cantilever oscillates.

The actual resonant frequency of the HR device was obtained by fixing the input sound pressure level, p_{in} , to 110 dB, while the input

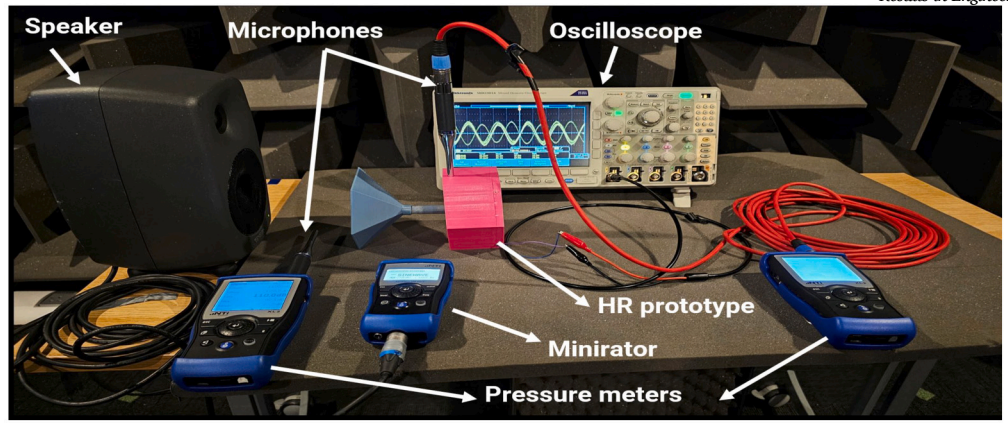


Fig. 4. The experimental set-up, showing the sensitive microphones, the sound pressure level measuring devices, the Minirator and an oscilloscope.

frequency is varied within the design range. The sound pressure amplitude inside the HR device was measured for each input frequency and the maximum amplitude was identified. Although, in principle, the frequency response of loudspeakers is not flat over a frequency range to produce a constant pressure amplitude, qualitative results are obtained by adjusting the sound pressure level relative to the acoustic pressure with the minirator. Consequently, the experimental investigation revealed an optimal resonant behaviour at a frequency, $\omega_{rex} = 110 \text{ Hz}$.

5. Results and discussion

5.1. Frequency response

First, we present the results obtained for the traditional resonance in Fig. 5. The frequency-response curve of the modelled HR unit described by Eq. (9), is shown in Fig. 5a. The system's analytical response, Q_{ana} , is compared with the numerically computed response, Q_{num} . The curves are clearly in good agreement. The influence of varying the amplitude of the acoustic external excitation, F, on the frequency response of the system is shown in Fig. 5b. Note that the values considered for the force amplitude, F = [0.0003, 0.0021, 0.0672, 0.1194, 0.2124],correspond to sound pressure levels, SPL (dB) = [95, 110, 140, 145, 150], respectively. The system response Q decreases with increasing F. It should be noted that F = [0.0672, 01194, 0.2124] are very high levels of sound pressure, and the peak shifts observed on the resonance curves are the typical hardening behaviour of the HR unit, when driven by a high force [30-32]. This is an important characteristic of HR models, which demonstrates that their dynamic behaviour is akin to that of a Duffing oscillator, where the nonlinear spring constant determines the softening or hardening behaviour of the system.

The dependence of the system response amplitude Q on F is shown in Fig. 6a, for four different values of the excitation frequency, $\Omega_f=[1.00,\,1.05,\,1.10,\,1.14]$. The figure depicts the variation of Q with increasing pressure amplitude, F, when the excitation frequency, Ω_f , is slightly varied around the characteristic resonant frequency. To unravel the underlying dynamical mechanism associated with the occurrence of acoustic resonance at distinct parameter values of the sound wave components, a three-dimensional graph of the relationship between the response amplitude, Q, and the amplitude of the sound wave F and its frequency Ω_f , is shown in Fig. 6b. The figure (Fig. 6b) clearly shows regimes of significant enhancement, as shown by Figs. 5b and 6a. With the peak in the range $0 < F \le 0.05$, it is clear that the system resonates effectively for F < 0.1. The red region indicates high response regimes for the sound pressure level, SPL > 84 dB but < 140 dB.

To further characterise the dynamic response of system (9), and validate both our numerical and theoretical results, we present the bifurcation diagram of the HR model in Fig. 7. Although the figures mimic those reported in [31], we emphasise that the results in this study are

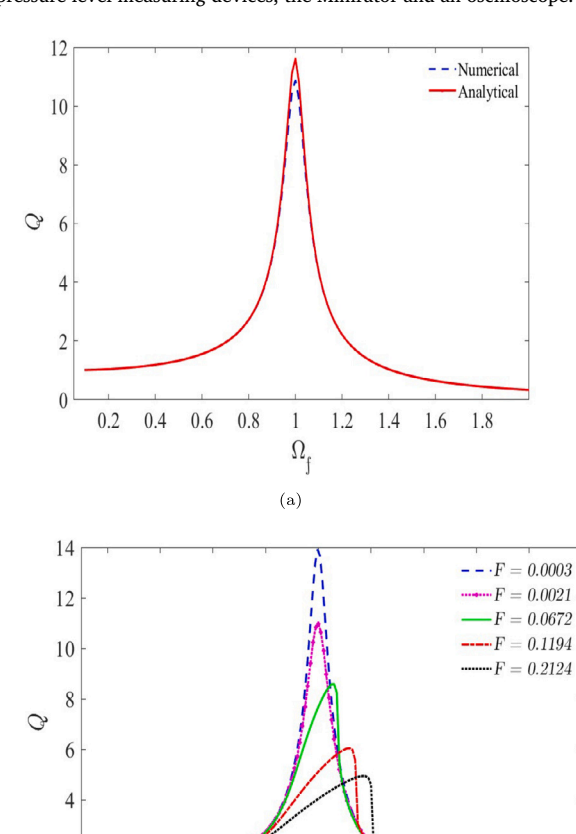


Fig. 5. (a) Frequency response curve, showing the dependence of response amplitude Q on the dimensionless frequency Ω_f . The solid red line represents the analytically-calculated Q_{ana} from Eq. (12), while the dashed blue line represents the numerically-computed Q_{num} from Eq. (15). (b) Dependence of Q on Ω_f , for five different values of the amplitude of the acoustic excitation, F = [0.0003, 0.0021, 0.0672, 0.1194, 0.2124].

(b)

0.8

0.4 0.6

0.2

1.2

 Ω_{f}

1.4

1.6

novel and distinct, since the dynamic response of the modelled HR system was obtained using realistic parameter values. First, we examine the effect of frequency variation on air molecule displacement in the HR cavity, in Fig. 7a. Here, it is clearly evident that increasing the value of Ω_f , changes the behaviour of the system. The implication is that the

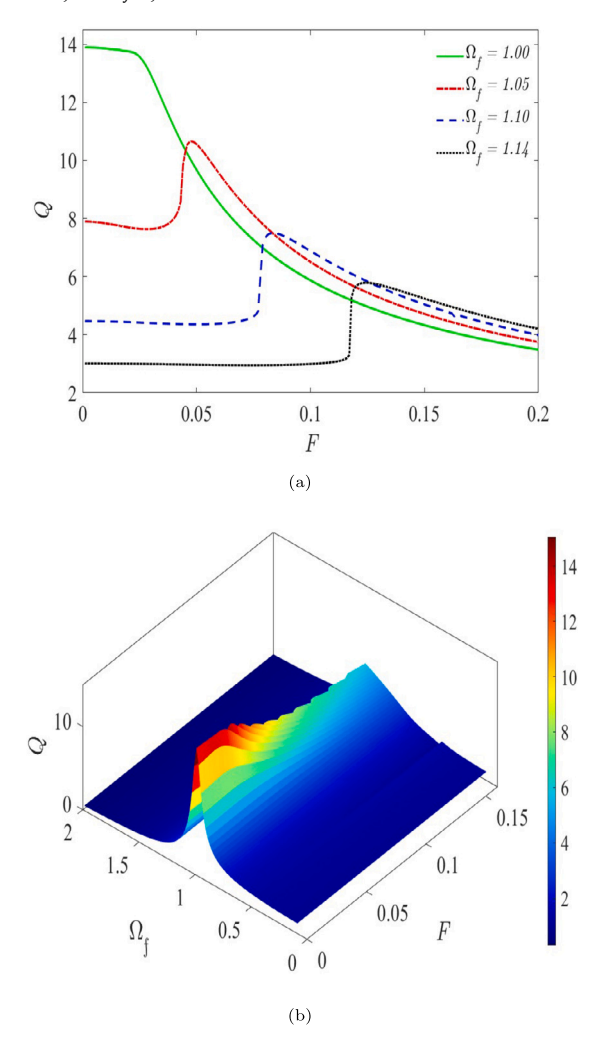


Fig. 6. (a) Dependence of the response amplitude Q on the amplitude F of the acoustic excitation, for four different values of the excitation frequency, $\Omega_f = [1.00, 1.05, 1.10, 1.15]$. (b) Surface plots of Q against Ω_f and F, showing that the system resonate effectively for F < 0.1, with the peak in the range $0 < F \le 0.05$. The red region indicates regimes of strong enhancement.

sensitivity of the system varies with frequency. Therefore, to discuss the possibility of initiating resonance from the system's parameters and the acoustic force, we categorised the influence of the excitation frequency, Ω_f into three stages; Stage I, Stage II and Stage III, in the range $0 < \Omega_f < 0.58$, $0.58 \le \Omega_f < 1.21$ and $\Omega_f > 1.21$, respectively. Our region of interest is Stage II. This is because our objective is to enhance the system response to weak acoustic excitations. Moreover, within the specified frequency range, $0.58 \le \Omega_f < 1.21$, which corresponds to 55.81 Hz $< \omega \le 116.44$ Hz, the displacement A_x of the system increases with increasing frequency. The displacement A_x of the system gradually increases and reaches its maximum value at 116.44 Hz, as the frequency of the external acoustic force increases from a low value. When Ω_f increases further, A_x jumps abruptly and discontinuously. Hence, it shows that the system exhibits a jump or hysteresis phenomenon. In particular, the measured resonant frequency ($\omega_{rex} = 110 \text{ Hz}$) from the experiments is also captured by the frequency range. The dimensionless value is shown in the figure (Fig. 7a), $\Omega_{rex} = 1.14$.

A bifurcation diagram provides a framework for understanding how small variations in the operating conditions of a nonlinear system can abruptly change its response. These nonlinear transitions, often undetectable in perturbation-based models like those used in acoustic energy harvesting (AEH), are crucial to predicting, controlling, and optimising performance. By directly analysing the full nonlinear dynamics, we re-

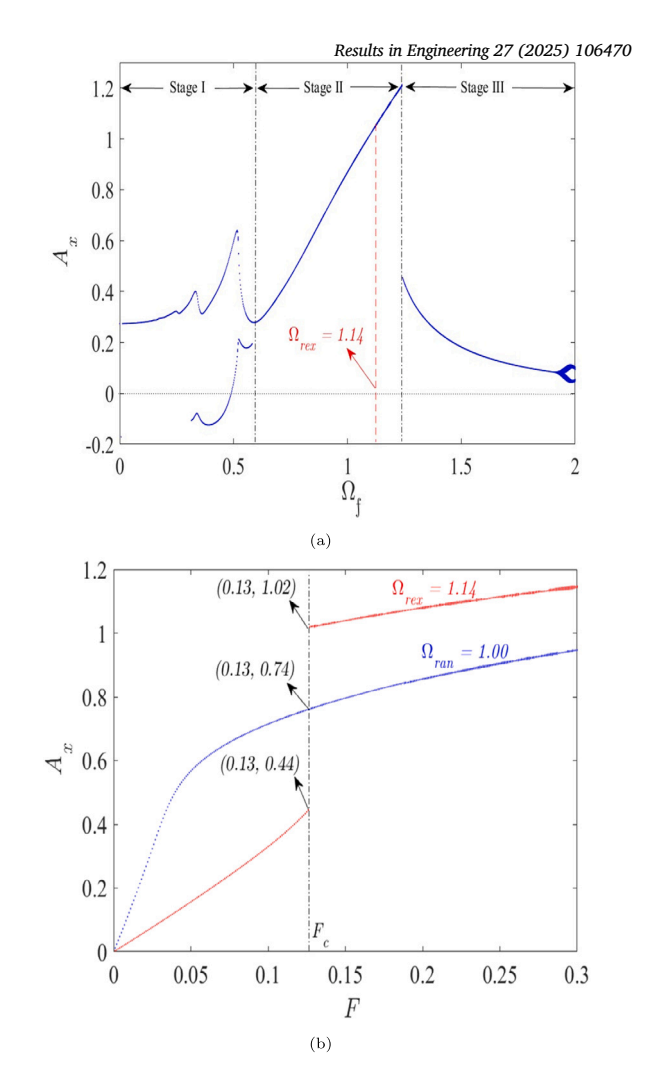


Fig. 7. Bifurcation diagram of the HR system (Eq. (9)) with, (a) increasing excitation frequency, Ω_f , when the amplitude of the acoustic wave F=0.2124; (b) increasing amplitude, F, while $\Omega_f=1.00$ and 1.15.

veal other hidden features of HR, and the bifurcation structures that govern the onset of jump phenomena and sensitivity of the system, all of which are essential features for next-generation AEH designs.

To further analyse the behaviour of the system, subject to changing values of the acoustic force parameters, Fig. 7b provides the bifurcation diagram for the variation of A_x with increasing amplitude of the sound wave F, for $\Omega_f = 1.00$ and 1.14, the dimensionless resonant frequency obtained analytically (Ω_{ran}) and experimentally (Ω_{rex}), respectively. Although the system response with Ω_{rex} is greater than that of Ω_{ran} , we observed that the behaviour of the system is similar for both frequency values, particularly, when F > 0.13. Moreover, the response at the lower values of F (F < 0.13) is higher for the analytical case. On the other hand, the dynamics of the HR unit, as predicted by our experimental model based on the measured value of the resonant frequency, Ω_{rex} , is very realistic. This is because at a relatively fixed frequency with low sound pressure level, it is possible to have a linear relationship between the response of the HR unit and the amplitude of the acoustic force. Otherwise, the sudden jump or sudden increase in displacement, A_x , when $F \ge 0.13$, can only be attributed to the complex nonlinear behaviour of the HR unit [30,31]. In other words, this could be the effect of the significant difference between the root mean square (rms) value of the acoustic pressure (p_{rms}) and its equivalent sound pressure level (SPL dB), at higher values. Therefore, F = 0.13 can be termed a critical pressure amplitude (F_c) . Subject to other physical and ambient conditions, this can be further analysed experimentally.

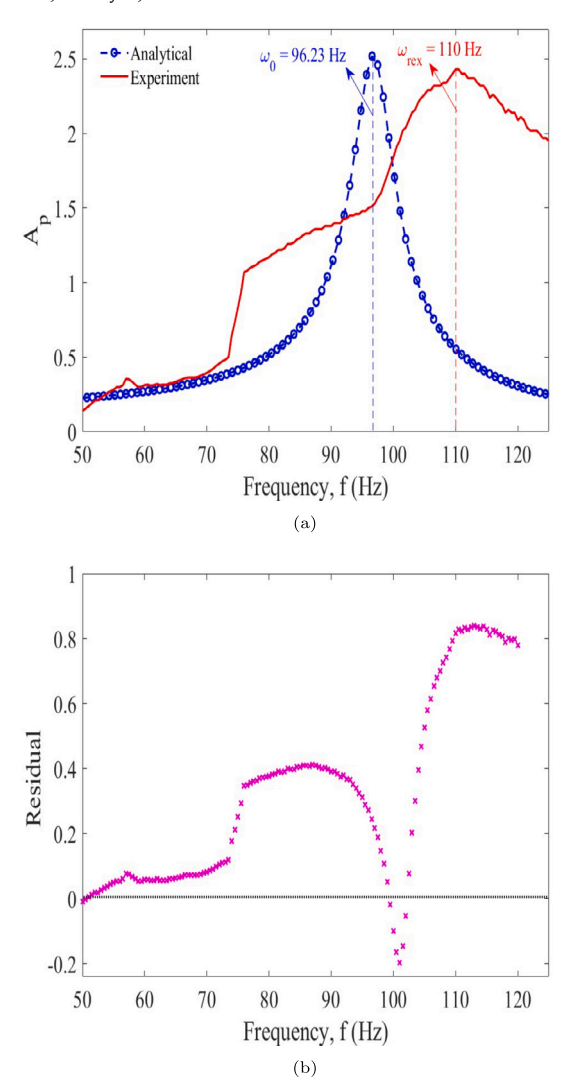


Fig. 8. (a) The superimposed response curve of the systems's amplification factor with changing frequency. The analytical curve is plotted with markers (dashed line), while the solid line represents the experimental curve. (b) Residuals between experimental and analytical amplification amplitude.

Next, we used the experimental data to characterise the resonance dynamics of our HR design. To gain a deeper insight into the resonance dynamics of the system, when subjected to an acoustic pressure, and highlight the novelty of our model in describing the response behaviour of the prototype HR unit, we compared the analytical response curve with the experimental curve. This is shown in Fig. 8a. Experimentally, this is achieved by computing the efficiency of the system in terms of the pressure amplification factor A_p , which is the ratio of the output sound pressure (p_{out}) of the HR unit to the input sound pressure (p_{in}) . The variation of the amplification factor A_n with frequency shows that the system exhibits a resonant behaviour at ω_{rex} , presented with a solid line in Fig. 8a. More so, we defined the amplification factor, A_p , by rescaling the analytical response amplitude, Q, such that, $A_p = \phi Q$, where $\phi = \frac{1}{\epsilon}$ was empirically fitted to align the theoretical response amplitude Q with the experimental amplification factor, A_p . This factor accounts for physical differences in units and domain. This approach is commonly adopted when comparing theoretical models to physical systems where direct analytical calibration is complex or impractical. This is plotted using a dashed line with markers, as shown in Fig. 8a. The comparison is logical, based on the typical assumption that the amplitude of the external acoustic pressure is proportional to the system's response amplitude, Q [30,31,65]. The observed frequency shift indicates that nonlinearity

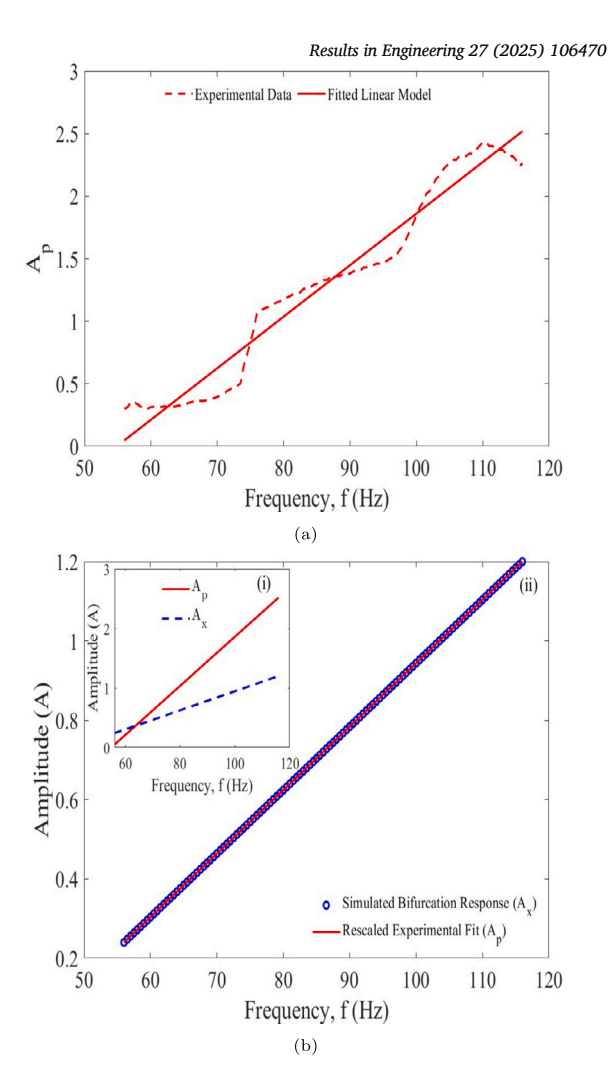


Fig. 9. (a) Linear fit of experimental amplification curve, with a least squares linear fit equation, $A_p = \lambda_1 f + \lambda_2$, where $\lambda_1 = 0.0412$, and $\lambda_2 = -2.2599$. (b) Comparison of fitted experimental response and simulated bifurcation trend, (i) unscaled amplitude and (ii) the rescaled system response with a least squares equation $A = \sigma_1 f + \sigma_2$, where $\sigma_1 = 0.3884$, and $\sigma_2 = 0.2217$.

increases with rising acoustic pressure. Furthermore, the classical theory describing the behaviour of air molecules inside an acoustic resonator assumes adiabatic conditions. Based on this, the Helmholtz number, H_e , is defined in terms of the neck length L_n , speed of sound c, and resonant frequency ω_r as:

$$H_e = \left(\frac{L_n}{c}\right) \omega_r$$

 is insignificant. Therefore, the difference between the theoretical and experimental resonant frequencies of the system can be attributed to other nonlinearities associated with the dynamics of the Helmholtz resonator. For example, in typical mass-spring-damper systems, such as the Duffing-type oscillators, nonlinearities increase the resonant frequency, thus widening the frequency range over which energy is harvested, especially at the high frequency range [39,41–43,73]. Such systems have been extensively studied and it has been established that ideally, a hardening stiffness configuration will generate the same maximum amount of power as a linear system but over a wide frequency range, depending on the degree of nonlinearity [73].

It should be noted that both the analytical and the experimental resonant frequencies, ω_0 and ω_{rex} , were captured at Stage II, as shown in Fig. 7a. It is worth mentioning that the occurrence of resonance, facilitated by the frequency variation and the excitation level of the air molecules in the HR's cavity, is controllable in Stage II, for efficient performances [31]. Meanwhile, it is also important to note that acoustic and mechanical resonances are inherent in HR structures, which could be observed at slightly different resonant frequencies [9,10]. Therefore, it is logical to assume that ω_0 , the analytical resonant frequency, only accounts for the associated mechanical effects on the system. However, Ω_{rex} is apparently the operational resonant frequency. Consequently, our modelled equation, system (9), can be used to predict the response dynamics of the HR unit. However, it would be curious to know the possibilities of taking advantage of the system's performance, particularly in Stage II, for improved acoustic energy harvesting. This is because the results can be promising and highlight the transformative potential of HR designs.

To validate the analytical model, we first compare its predictions with experimental results by analyzing the residuals, as shown in Fig. 8b. The residual plot reveals a systematic deviation, highlighting a shift in the resonance peak between the model and experiment. Positive residuals dominate at higher frequencies (above 100 Hz), indicating that experimental amplitudes exceed theoretical predictions, particularly near the experimental resonance at 110 Hz. Conversely, a negative dip around 96–100 Hz, where the theoretical model peaks, confirms a misalignment in resonance peaks or a potential phase shift in the analytical response.

Despite these discrepancies, the overall trend indicates that the model remains structurally sound and captures the system's dynamic behaviour, especially in the amplification and resonance regimes. To assess the validity of a linear approximation, we focused on the frequency range of 55.81–116.44 Hz, where the system exhibits a near-proportional response. Fig. 9a shows the linear fit of the experimental data, represented by a continuous line, while Fig. 9b provides a direct comparison between the fitted experimental response and the simulated bifurcation trend. Fig. 9b(i) presents unscaled amplitude variations (A_x and A_p), and Fig. 9b(ii) shows the rescaled response using the least squares fit:

$$A = \sigma_1 f + \sigma_2$$
, where $\sigma_1 = 0.3884$, $\sigma_2 = 0.2217$.

The experimentally fitted response was rescaled to match the amplitude bounds in the bifurcation diagram. The resulting trend closely follows the simulated response, suggesting strong alignment between experimental observations and the expected dynamic behaviour under increasing excitation frequency. Quantitative comparison over this regime yielded a root mean square error (RMSE) of 0.1484, a mean absolute error (MAE) of 0.1300, and a coefficient of determination (R^2_{error}) of 0.9582, confirming strong agreement and validating the linear assumption within this bandwidth.

Finally, it is important to note that resonance behaviour, influenced by frequency variation and the excitation levels of air molecules within the HR cavity, remains highly controllable in Stage II. This controllability provides a useful mechanism for optimising acoustic energy harvesting in real-world applications [31]. This foundation enables the

exploration of new pathways for addressing resonance-induced industrial and environmental acoustic challenges. In the next section, we discuss and analyse acoustic energy harvesting using our Helmholtz resonator (HR) design.

5.2. Acoustic energy harvesting

To facilitate optimal acoustic energy harvesting with our HR design, a piezoelectric PVDF film was integrated into the system, as shown in Fig. 3. For electrical power generation, the PVDF film was configured as a cantilever beam—rigidly fixed at one end to the base of the Helmholtz resonant cavity, with the other end left free to vibrate in response to the acoustic pressure field. This setup establishes a classic fixed–free boundary condition. Mechanical coupling was ensured by securely mounting the clamped end of the PVDF to the inner base surface of the cavity, allowing the film to respond directly to the cavity's resonant acoustic excitation.

This simple, uniform cantilever configuration was chosen not only for its physical effectiveness but also for its suitability for analytical modelling. As illustrated in Fig. 10c, the design supports tractable theoretical analysis of the electromechanical response under varying excitation frequencies. Note that it has been established in the literature [74,75] that a single-layer piezoelectric cantilever vibrates in response to external excitation. Under resonant conditions, the resulting mechanical strain and bending effect lead to the generation of electric energy.

A piezoelectric film can produce electricity in either the 31-piezoelectric mode or the 33-piezoelectric mode, depending on whether the polarization and external forces move in the same or opposite directions. The amplified air pressure inside the HR cavity excites the piezoelectric cantilever installed at the base of the cavity, causing it to vibrate at its resonant frequency. This is because the resonant frequency of the HR structure has been designed to match that of the piezoelectric strip. The vibration of the piezoelectric strip leads to the generation of electric energy. The piezoelectric film used in this study is operated in the 31 mode. Some basic properties of the piezoelectric film are provided in Table 2 [44].

5.2.1. Dynamics of the piezoelectric cantilever with acoustic pressure

Here, we present the constitutive analytical equation, the numerical simulation, and the systematic description of the piezoelectric configuration. Accordingly, the equation for the operation of the piezoelectric film in the 31-modes is

$$S_{1} = s_{11p}^{E} T_{1} + d_{31} E_{3}$$

$$D_{3} = d_{31} T_{1} + \epsilon_{33}^{T} E_{3},$$

$$(18)$$

where S_1 is the strain, T_1 is the stress directed towards the length of the piezoelectric layer; E_3 and D_3 are the electric field and electric displacement, respectively; ϵ_{33}^T is the permittivity at constant stress of the piezoelectric layer, and d_{31} is the transverse piezoelectric coefficient [53].

Several mathematical models of vibrating beams are useful in describing the dynamics of energy harvesting systems, using piezo-electric films [5]. The response of a piezoelectric cantilever strip to low-frequency vibrations is also important and can be obtained using Eq. (18). In addition, the equation is useful for understanding the general behaviour of a piezoelectric cantilever. However, most models only predict the first vibration mode of the beam, since some components of the electromechanical coupling of piezoelectric devices [7,45] are ignored when simplified models are considered. Researchers have looked into distributed parameter models using Rayleigh-Ritz discretisation, which offers more accurate solutions than lumped-parameter models. Using Euler-Bernoulli beam theory, researchers have also sought to create precise analytical solutions for the piezoelectric cantilever harvester [5,53].

Consequently, this study utilises the simple uniform cantilever arrangement for the acoustic energy harvesting, described in Fig. 10. The

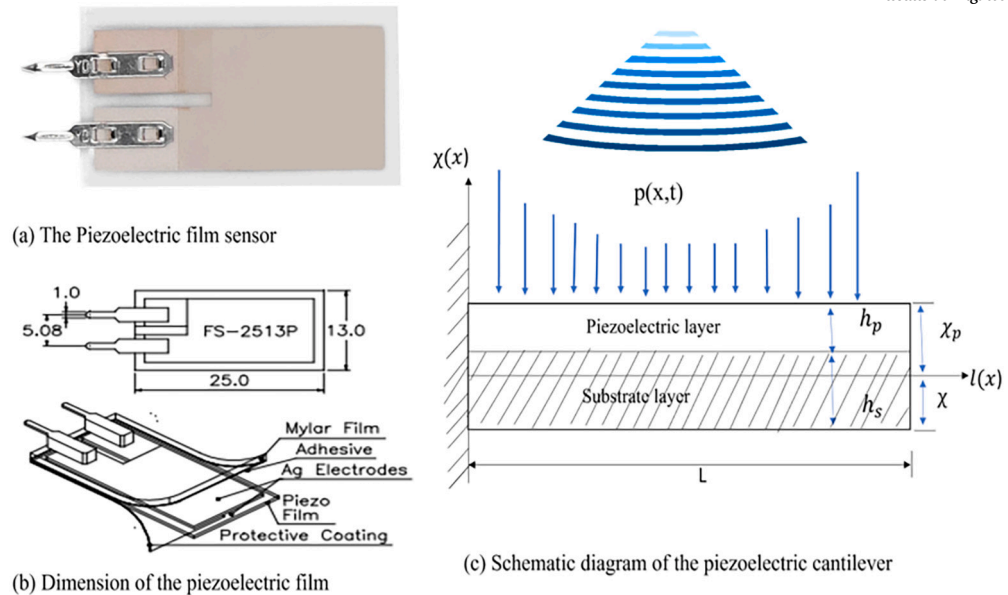


Fig. 10. Features of the energy transducer; (a) the piezoelectric film sensor (model FS-2513P), and (b) the dimension of the sensor. (c) Schematic diagram of the piezoelectric cantilever.

Table 2
Summarised parameter values of the PVDF film (www.midascomponents.co. uk).

| Parameter | Value |
|------------------------------------|-----------------------|
| Width w | 13.0 mm |
| Height h | 25.0 mm |
| Thickness | 0.2 mm |
| Piezo strain constant d_{31} | 23 pC/N |
| Damping ratio ζ | 0.05 |
| Coupling factor κ | 0.14 |
| Relative permittivity ϵ_r | 12 - 13 |
| Young's Modulus Y | 2 – 4 GPa |
| Capacitance C_p | 380 pF/cm^2 |

configuration facilitates a straightforward analytical solution. The cross-section of the Polyvinylidene Fluoride (PVDF) film and its dimensions are shown in Figs. 10a and 10b, respectively. Moreover, some basic properties of the piezoelectric film [44] are shown in Table 2. Hence, assuming all of the harmonic loadings on the piezoelectric cantilever are uniform, the displacement, χ , which is the measured separation between the neutral plane and the beam's bottom surface, can be written as [53]

$$\chi = \frac{E_{Ys}h_s^2 + s_{11p}^E h_p^2 + 2s_{11p}^E h_p h_s}{2(s_{11}^E h_p + E_{Ys}h_s)},\tag{19}$$

where h_p is the thickness of the piezoelectric material and h_s is the thickness of the substrate material. The elastic constant of the substrate is represented by E_{Ys} , while s_{11p} is the elastic compliance at constant electric field.

The mechanical displacement of the cantilever under acoustic excitation induces strain along the PVDF film. Owing to the piezoelectric effect, this strain generates an electric field within the material, resulting in a measurable voltage across its electrodes. This electromechanical coupling forms the basis for predicting the voltage output of the system. Thus, the induced voltage, as obtained in [53], can be calculated from

$$I_{p} = \omega(VC_{0} + A_{p}p_{in}\tau_{p})$$

$$|V_{oc}| = \kappa A_{p}p_{in}$$
(20)

 τ_p is the coupling factor between the induced electric charge and the applied voltage. The harmonic excitations due to the amplified acoustic field yielded κ , the sensitivity of the open-circuit voltage. p_{in} and A_p are the input acoustic pressure and the HR's amplification factor, respectively.

Generally, the natural frequency of the piezoelectric cantilever and the spatial solutions of the beam's eigenfunction modes, shapes, and the eigenvalue roots can be computed from [76]

$$f_n = \frac{\beta_n^2}{2\pi} \sqrt{\frac{\delta_n}{m_0}}.$$
 (21)

Interestingly, the number β_n depends on the boundary conditions and consequently, it imposes the task of finding values that satisfy the resonance equation. This implies that each distinctive value is expected to have a unique natural resonant frequency. To ease this task, one can also express the frequency equation, (Eq. (21)) in an elegant form, by putting into consideration the length of the cantilever beam, in the form

$$f_n = \frac{(\beta_n L)^2}{2\pi L^2} \sqrt{\frac{\delta_n}{m_0}},\tag{22}$$

such that the first five possible non-dimensional eigenvalues for the fundamental vibration mode are 1.8753, 4.6941, 7.8548, 10.9955 and 14.1372, for n = 1, 2, 3, 4 and 5, respectively [53,76].

Usually, the goal is to modulate the resonant frequency of the bilayer piezoelectric cantilever, Eq. (22), to match the fundamental frequency of the resonating air molecules in the cavity (Eq. (14)), so that, the piezoelectric film can vibrate optimally to generate maximum power. The most important aspect is that the loading effect on the piezoelectric cantilever depends on the pressure in the HR's cavity, which is proportional to the ambient acoustic force. This implies that the vibration of the cantilever increases over time with increasing amplitude of the external acoustic pressure. The variation of the induced voltage, $|V_{oc}|$ with the dimensionless frequency, Ω_f , computed analytically using Eq. (20) is shown in Fig. 11. The figure presents the effect of varying amplitude of the input sound pressure (F) on $|V_{oc}|$. It is evident that as the amplitude grows, so does the generated voltage. Interestingly, Fig. 11a displays the induced voltage with the high pressure values (F = [0.0672, 0.1194, 0.2124]) in the macro-scale, whereas Fig. 11b displays the voltage in the micro-scale, with F = [0.0003, 0.0021].

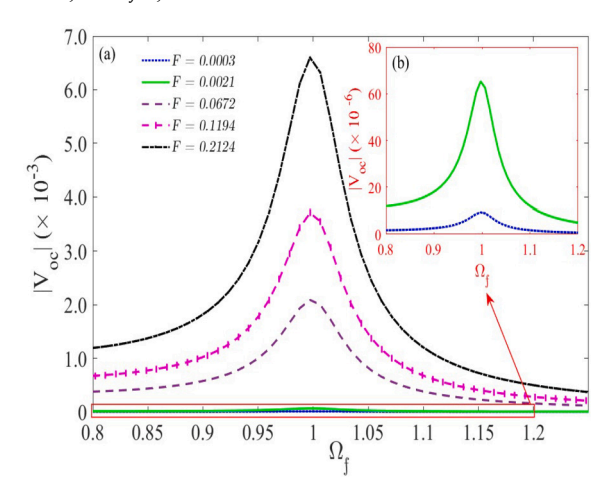


Fig. 11. Dependence of the induced voltage, $|V_{oc}|$ on the dimensionless frequency Ω_f , computed using Eq. (20) for different amplitude of the external acoustic pressure, F = [0.0003, 0.0021, 0.0672, 0.1194, 0.2124].

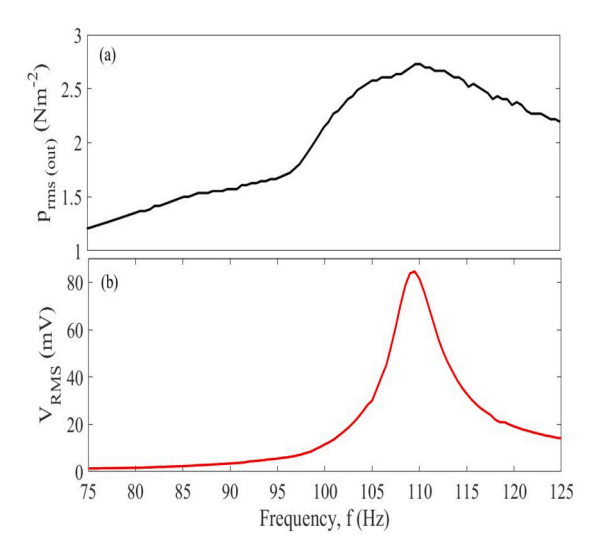


Fig. 12. The frequency-response curve of the acoustic energy harvester in stage II; (a) variation of the output sound pressure, p_{out} (Nm⁻²) of the HR, with increasing frequency, and (b) the dependence of the induced RMS-voltage on the frequency of the acoustic wave.

Next, we present our control experiment results in Fig. 13, which establish the resonant frequency of the piezoelectric film and provide a baseline for comparison. By varying the distance d between the sound source and the film, we minimized experimental bias and strengthened the credibility and reproducibility of our findings.

Fig. 13 shows the dependence of generated voltage on d at a constant frequency ($f=110\,$ Hz), both with and without the Helmholtz resonator. At the closest distance ($d=0.025\,$ m), the film produces appreciable voltage in both configurations, with peak voltages $V_{\rm max}$ of 84.2 mV (with HR) and 21.0 mV (without HR). This fourfold increase in voltage output when using the HR demonstrates its effectiveness, even as d increases, the resonator-enabled configuration continues to harvest significant energy, whereas the output without the HR rapidly diminishes. These results validate the practical efficiency of our HR design under realistic acoustic conditions.

To further demonstrate the robustness of our experimental approach, we varied the sound-wave frequency while keeping the source–film separation d fixed. Fig. 14a shows the superimposed voltage–frequency curves for d=[0.025,0.05,0.10,0.15] m. Together with the distance-dependence data in Fig. 13, these results confirm the consistency and reproducibility of our measurements. The voltage response curves main-

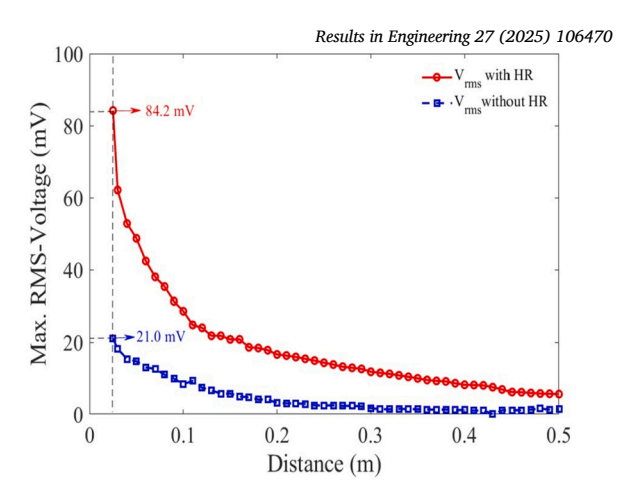
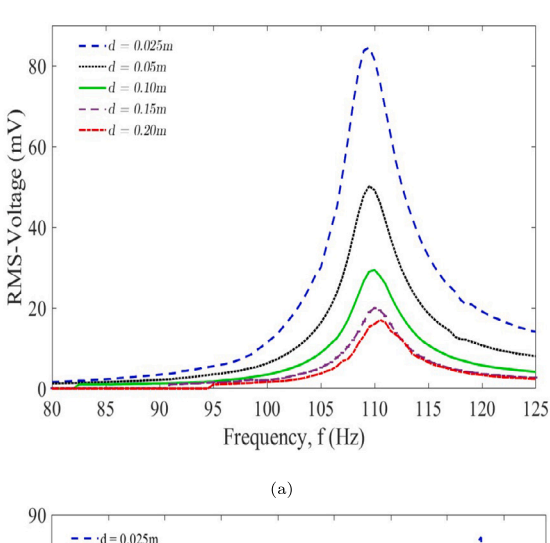


Fig. 13. Performance of the piezoelectric film at varying distances from the acoustic source with and without HR.



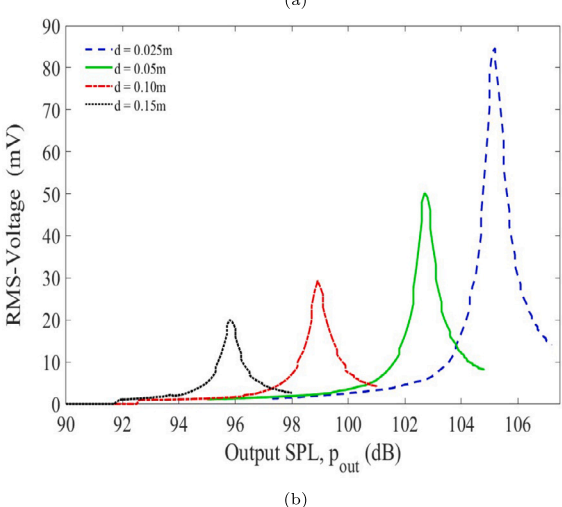


Fig. 14. (a) The superimposed voltage curves as a function of frequency for different separation distances, $d=[0.025,\ 0.05,\ 0.10,\ 0.15,\ 0.20]$ (m), with a fixed input sound pressure level, $p_{in}=95$ dB. (b) The superimposed response plots of the generated voltage, V as a function of sound pressure level, (SPL) with varying distance, $d=[0.025,\ 0.05,\ 0.10,\ 0.15,\ 0.20]$ (m) at constant frequency, f=110.

tain their characteristic shape and relative magnitudes across all tested distances.

To further examine the effect of the separation distance between the sound source and the HR on the performance of the AEH, we plotted

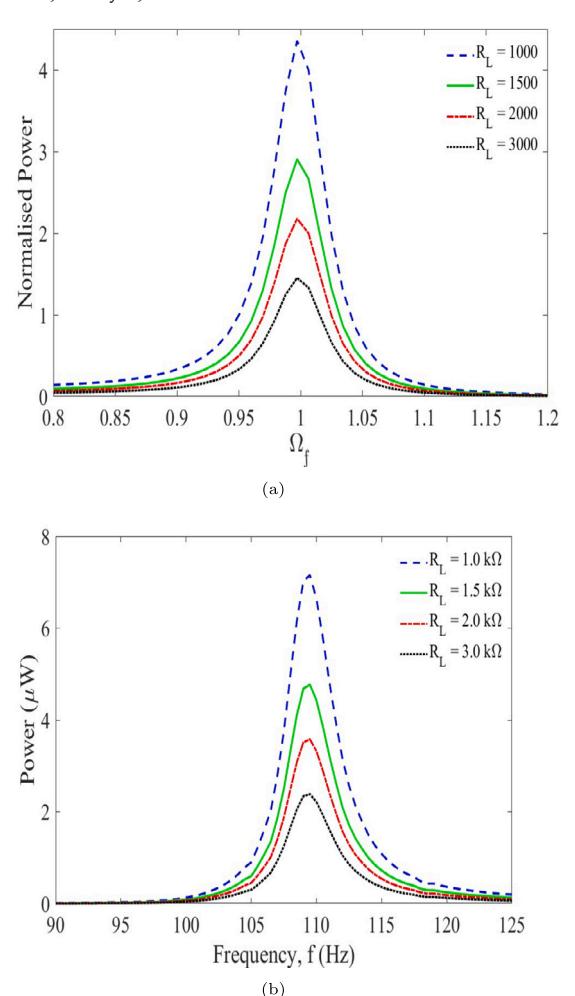


Fig. 15. (a) Variation of the harvested power with frequency for different dimensionless load resistances, R_L ($R_L = [1000, 1500, 2000, 3000]$), computed using Eq. (20) and Eq. (23). (b) The experimental dependence of the generated power on frequency for varying load resistance, R_L ($R_L = [1.0, 1.5, 2.0, 3.0]$ k Ω).

the dependence of the generated voltage, V_{rms} on output sound pressure level, p_{out} for four different distances, d = [0.025, 0.05, 0.10, 0.15] (m) in Fig. 14b. This is achieved by fixing both the input sound pressure level and the frequency. The figure (Fig. 14b) further confirms the prediction of increased voltage with a high acoustic amplitude in Fig. 12a. The implication is that the magnitude of the incident acoustic pressure determines the resultant output voltage generated by the AEH.

5.3. Power extracted by the AEH

Power extracted by the AEH is used as a performance metric, to measure the functionality of the design. To complement our findings and measure the energy harvesting capability of the AEH device, the piezoelectric film was connected to a resistance box in series, and the external resistance was equal to the source impedance of the piezoelectric patch to extract maximum power. Thus, the harvested power can be calculated from [77]

$$P_e = \frac{V_{RMS}^2}{R_L},\tag{23}$$

where R_L is the load resistance in Ohms (Ω). We estimated the power generated by the system analytically, when a load resistance, R_L is connected. The variation of the power with frequency for different dimensionless load resistances, R_L ($R_L = [1000, 1500, 2000, 3000]$), computed using Eq. (20) and Eq. (23) is shown in Fig. 15a. The experimental

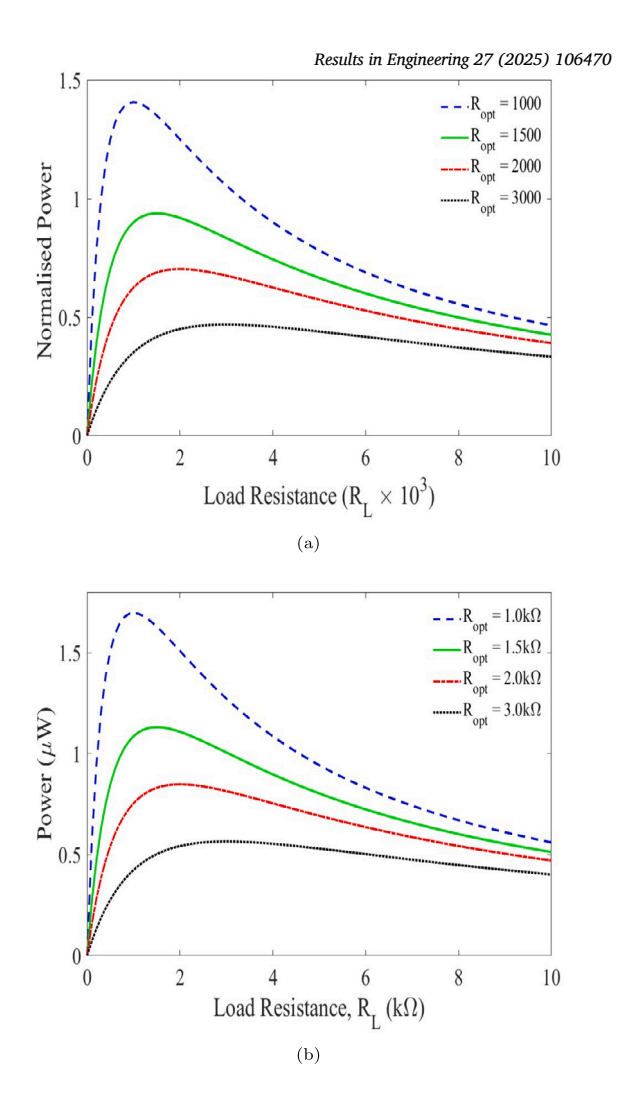


Fig. 16. (a) The harvested optimal power variation with load resistance, R_L for different dimensionless optimal resistances, R_{opt} (R_{opt} = [1000, 1500, 2000, 3000]), calculated using Eq. (20) and Eq. (23). (b) The plots of the experimentally harvested optimal power as a function of load resistance, R_L for different optimal resistances, R_{opt} (R_{opt} = [1.0, 1.5, 2.0, 3.0]kΩ).

dependence of the generated power on frequency for varying load resistance, R_L ($R_L = [1.0, 1.5, 2.0, 3.0] \mathrm{k}\Omega$) is presented in Fig. 15b. It is evident from Fig. 15 (both Fig. 15a and Fig. 15b) that the power output exhibits a sharp peak at the resonant frequency, indicating maximum energy harvested by the AEH at resonance. The system achieved 7.50 μ W maximum power with a 1.0 $\mathrm{k}\Omega$ load resistance, at resonance.

Also, we evaluated the design using normalized power density, achieving a maximum of $0.015~\mu \text{W/cm}^3$. Although our analysis focuses on a single PVDF film within the resonator cavity, the prototype's performance suggests that harvested energy could be substantially increased by installing multiple films or by arraying several AEH units. This scalability highlights the reliability and potential of our design for applications such as standby power along rail lines or low-power electronic devices. For example, Wang et al. [44] demonstrated significant electricity generation by deploying multiple AEH units in arrays along high-speed rail tracks.

Fig. 16 shows the variation of the generated power with different load conditions. Since external pressure increment, resonant frequency, and the piezoelectric film's capacitance all affect the ideal power generated with fixed resistance [10,77], the measured optimal resistance may vary for any given situation. The theoretical and experimental results on the harvested power are shown in Figs. 16a and 16b, respectively. The variations are exactly in the same manner. The maximum harvested

Table 3Comparison of the harvested power by AEHs that utilises HR units.

| Reference | Incident SPL (dB) | Sound pressure (Pa) | Volume of harvester (cm ³) | Frequency (Hz) | Harvested power (μW) | Metric μW/ Pa ² .cm ³ |
|-----------|----------------------|------------------------|---|---|-------------------------|--|
| [9] | 130 | 63.25 | 13.12 | 1453 - 1542 1710 - 1780 1848 - 1915 | 214.23 | 0.004 |
| [10] | 100 | 2 | 200 | 217 (Acous. resonance) 341 (Mech. resonance) | 27.2 64.4 | 0.034 0.0805 |
| [15] | 100 | 2 | 3972.22 | 170 - 206 | 137 - 1430 | 0.0089 - 0.09 |
| [19] | 100 | 2 | 19.44 | 2257.5 | 8.8 | 0.1132 |
| [20] | 114 | 10 | 2.133 | 155 | 210 | 0.985 |
| [46] | 100 | 2 | 251 | 175 | 7.3 | 0.0072 |
| [53] | 145.5 | 376 | 55.5 | 834 | 0.094 | 1.198×10^{-8} |
| [54] | 100 | 2 | - | 401 | 100.8 | - |
| [55] | 114 | 10 | 11.66 | 2722 | 93.13 | 0.079 |
| [58] | 94 | 1 | - | 550 | 520 | - |
| This work | 95 | 1.12 | 500 | 110 | 7.5 | 0.012 |

power was obtained with the $R_{\it opt}=1 \rm k\Omega$. To maximize harvested power, load matching is crucial, as shown by the power–load resistance characteristics in Fig. 16. For effective energy extraction in real-world sensor networks and Internet of Things applications, where power budgets are often limited [78], selecting the appropriate load resistance (or employing adaptive impedance-matching circuits) is essential. Different sensors and modules have varying input impedances, and any deviation from the optimal resistance can drastically reduce available power, adversely affecting node uptime, data transmission reliability, or sensing accuracy. To ensure reliable and sustainable operation in autonomous or intermittently powered systems, it is important to understand and adjust the load resistance accordingly.

Building on the importance of optimal load matching, our results demonstrate that the proposed AEH device provides a notably more compact solution for low-frequency acoustic harvesting than earlier designs. Moreover, even when limited to a single HR unit, our system outperforms several previous studies in this frequency range, despite the inherently low power density metrics, highlighting both its efficiency and practical advantage for space-constrained applications.

We further evaluated our AEH design by calculating its energy harvesting efficiency using output power per unit area (ξ) and logarithmic power sensitivity (η). The efficiency, ξ that describes the output power per unit area, harnessed by the AEH when a load resistance R_L is connected to the harvester, can be expressed as

$$\xi = \frac{P_e}{A}.\tag{24}$$

Also, to characterise how efficiently the prototype device converts sound energy into electrical power, we defined the logarithmic power sensitivity, η as the ratio of the output electrical power $P_{e_{out}}$ to the input acoustic power $P_{e_{in}}$, such that the logarithmic power sensitivity can be written as

$$\eta = 10\log_{10}\left(\frac{P_{e_{out}}}{P_{e_{in}}}\right). \tag{25}$$

The variation of these performance metrics, ξ and η , with changing frequency of the incident sound wave is plotted in Fig. 17a and Fig. 17b, respectively.

In Fig. 17a, a sharp response peak is observed at the resonant frequency, 110 Hz, reaching a maximum of approximately $8\,\mu \text{W/cm}^2$. This indicates a strong resonance at that frequency where energy harvesting is most efficient per unit area. Outside the peak, power density is nearly zero, showing the sensitive of the system to frequency band. Additionally, in Fig. 17b, a smooth and stretched peak occurs, covering a wide frequency range (95 – 120 Hz), with a maximum sensitivity of around 38 dB. The logarithmic power sensitivity increases gradually with frequency up to resonance and then decreases, showing the ability of the device to convert acoustic power into electrical power efficiently. The

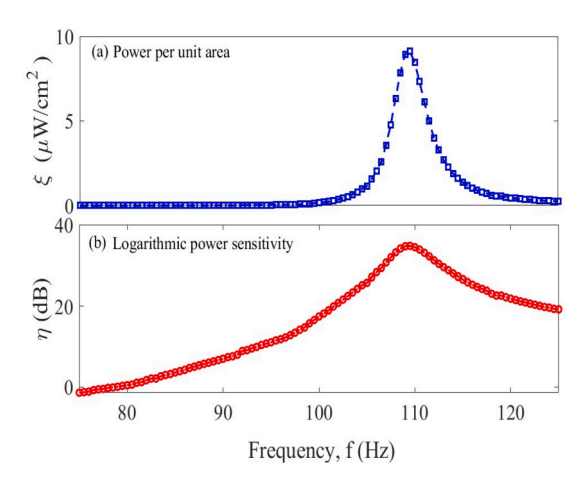


Fig. 17. Efficiency plots of the system as a function of frequency; (a) variation of power per unit area with frequency, and (b) the variation of the system's sensitivity.

broader curve suggests this metric is less sensitive to slight frequency shifts than the raw power per unit area. This shows the robustness and effectiveness of our designed HR in amplifying the incident sound wave, and indicates high efficiency of the prototype AEH.

On the other hand, it is important to mention that typically, most resonant energy harvesters have limited operational bandwidth [60,73], which our design is one. Hence, this accounts for the sharp peak in ξ with small bandwidth but high efficiency. Therefore, η (dB) provides a more robust indicator for real-world conditions, where slight detuning may occur. The implication is that our prototype AEH is ideal for targeted acoustic environments, such as machinery with fixed noise frequencies, aircraft or railway noise. To illustrate further, Table 3 lists the differences between the reported AEHs and our fabricated AEH based on a number of characteristics, including SPL, device size, resonant frequencies or bandwidth, output power, and power density.

6. Conclusion

The design of high-performance acoustic energy harvesting devices for the low-frequency regime remains a significant research priority. This study investigated the behaviour of a Helmholtz resonator (HR) prototype and demonstrated its ability to amplify sound pressure at its resonant frequency, which was demonstrated both analytically (ω_0 at 96.23 Hz) and experimentally (Ω_{rex} at 110 Hz). A set of sound pressure values, F_c , was identified, below which the HR's response amplitude increased linearly with the external acoustic force without shifting the resonant frequency. These findings confirmed that the HR effectively enhanced sound amplification at a single resonant frequency while ab-

sorbing acoustic waves at other frequencies. Aside from the chaotic and complex dynamics of the HR system reported in Refs. [30,31], we demonstrated that the system also exhibited jump or hysteresis behaviour at higher acoustic pressure.

The system exhibited amplitude magnification at the jump point, which both increases strain on the harvesting diaphragm and boosts power output. This behaviour offers two key advantages, which are (i) Nonlinear resonance amplification: Enhances energy harvesting performance near critical operational points. (ii) Broadband operation via bistability: Hysteresis supports multiple stable states over a frequency range, widening the effective harvesting bandwidth [6–8,79]. This is especially beneficial in real-world environments with fluctuating acoustic sources.

To further explore the HR potential, a piezoelectric Polyvinylidene diFluoride (PVDF) cantilever film, was integrated into the system for energy harvesting purposes. A significant amount of energy was generated with the HR, about four times the value without the resonator. By tuning the mechanical resonance of the piezoelectric cantilever, to align with the HR's acoustic resonance, the fabricated acoustic energy harvester (AEH) generated a peak output of 84.2 mV at Ω_{rex} with a fixed input sound pressure level (SPL) of 95 dB at a close range. The integration of the piezoelectric strip demonstrated the feasibility of using the HR device for rail-related noise control and as an alternative energy source to power low-voltage devices.

In conclusion, this study establishes the Helmholtz resonator as an effective and sustainable system for acoustic energy harvesting, with broad potential applications in noise control and low-power energy solutions. The single-unit Acoustic Energy Harvester (AEH) prototype demonstrated a normalized power density of approximately 0.015 µW/cm³ and a power sensitivity of 38 dB, yielding a measured output of about 7.5 µW under resonant acoustic excitation. While modest, this output is sufficient to intermittently operate or trickle-charge ultralow-power IoT devices, such as Bluetooth low energy (BLE) beacons or wireless temperature, humidity, and vibration sensors with average power consumption below 10 µW, by leveraging duty-cycled operation and energy storage (e.g., supercapacitors). A practical deployment scenario involves integrating AEH arrays into acoustic noise barriers along high-speed rail lines or within tunnel walls, where passing trains generate ambient acoustic energy. The system's compact, low-maintenance, and non-intrusive design supports scalable integration, enabling distributed powering of trackside monitors, environmental sensors, or fault detection units. While a single unit's output is limited, array configurations present a viable pathway for real-world applications. Future work will focus on analysing acoustic wave absorption within the system boundaries using advanced numerical simulation techniques to optimise transducer efficiency, broadband response, and system integration under diverse field conditions.

CRediT authorship contribution statement

K.A. Omoteso: Writing – review & editing, Writing – original draft, Software, Methodology, Investigation, Formal analysis. R. Marjani: Writing – review & editing, Writing – original draft, Methodology, Investigation, Formal analysis. O. Ozioko: Writing – review & editing, Writing – original draft, Supervision, Resources, Project administration, Formal analysis. O. Bagdasar: Writing – review & editing, Writing – original draft, Supervision, Resources, Project administration, Formal analysis. T.O. Roy-Layinde: Writing – review & editing, Software, Methodology, Investigation, Formal analysis. U.H. Diala: Writing – review & editing, Writing – original draft, Validation, Supervision, Software, Resources, Project administration, Methodology, Investigation, Formal analysis, Conceptualization.

Declaration of competing interest

The authors declare that they have no known competing financial interests or personal relationships that could have appeared to influence the work reported in this paper.

Data availability

Data will be made available on request.

References

- J. Choi, I. Jung, C.-Y. Kang, A brief review of sound energy harvesting, Nano Energy 56 (2019) 169–183.
- [2] P.D. Mitcheson, E.M. Yeatman, G.K. Rao, A.S. Holmes, T.C. Green, Energy harvesting from human and machine motion for wireless electronic devices, Proc. IEEE 96 (2008) 1457–1486
- [3] G. Ramkumar, S. Kannan, V. Mohanavel, S. Karthikeyan, A. Titus, The future of green mobility: a review exploring renewable energy systems integration in electric vehicles. Results Eng. (2025) 105647.
- [4] S. Matova, R. Elfrink, R. Vullers, R. Van Schaijk, Harvesting energy from airflow with a michromachined piezoelectric harvester inside a Helmholtz resonator, J. Micromech. Microeng. 21 (2011) 104001.
- [5] M. Safaei, H.A. Sodano, S.R. Anton, A review of energy harvesting using piezoelectric materials: state-of-the-art a decade later (2008–2018), Smart Mater. Struct. 28 (2019) 113001.
- [6] C. Wei, X. Jing, A comprehensive review on vibration energy harvesting: modelling and realization, Renew. Sustain. Energy Rev. 74 (2017) 1–18.
- [7] A. Aabid, M.A. Raheman, Y.E. Ibrahim, A. Anjum, M. Hrairi, B. Parveez, N. Parveen, J. Mohammed Zayan, A systematic review of piezoelectric materials and energy harvesters for industrial applications, Sensors 21 (2021) 4145.
- [8] D. Zhu, M.J. Tudor, S.P. Beeby, Strategies for increasing the operating frequency range of vibration energy harvesters: a review, Meas. Sci. Technol. 21 (2009) 022001.
- [9] Izhar, F.U. Khan, Three degree of freedom acoustic energy harvester using improved Helmholtz resonator, Int. J. Prec. Eng. Manuf. 19 (2018) 143–154.
- [10] M. Yuan, Z. Cao, J. Luo, Z. Pang, Low frequency acoustic energy harvester based on a planar Helmholtz resonator, AIP Adv. 8 (2018).
- [11] M. Meissner, The response of a Helmholtz resonator to external excitation. Part II: flow-induced resonance, Arch. Acoust. 30 (2005).
- [12] G. Catapane, D. Magliacano, G. Petrone, A. Casaburo, F. Franco, S. De Rosa, Semianalytical estimation of Helmholtz resonators tuning frequency for scalable neckcavity geometric couplings, CEAS Aeronaut. J. 13 (2022) 797–808.
- [13] D.K. Singh, S.W. Rienstra, A systematic impedance model for non-linear Helmholtz resonator liner, in: 19th AIAA/CEAS Aeroacoustics Conference, 2013, p. 2223.
- [14] K. Förner, M.A. Temiz, W. Polifke, I.L. Arteaga, A. Hirschberg, On the non-linear influence of the edge geometry on vortex shedding in Helmholtz resonators, in: Proceedings of the 22nd International Conference on Sound and Vibration, 2015–1341, 2015.
- [15] A. Yang, P. Li, Y. Wen, C. Lu, X. Peng, W. He, J. Zhang, D. Wang, F. Yang, Note: high-efficiency broadband acoustic energy harvesting using Helmholtz resonator and dual piezoelectric cantilever beams, Rev. Sci. Instrum. 85 (2014).
- [16] Q. Lu, X. Li, X. Zhang, M. Lu, Y. Chen, Perspective: acoustic metamaterials in future engineering, Engineering 17 (2022) 22–30.
- [17] H. Xiao, T. Li, L. Zhang, W.-H. Liao, T. Tan, Z. Yan, Metamaterial based piezoelectric acoustic energy harvesting: electromechanical coupled modeling and experimental validation, Mech. Syst. Signal Process. 185 (2023) 109808.
- [18] Q. Zhang, Z. Xi, Y. Wang, L. Liu, H. Yu, H. Wang, M. Xu, Multi-tube Helmholtz resonator based triboelectric nanogenerator for broadband acoustic energy harvesting, Front. Mater. 9 (2022) 896953.
- [19] S. Qi, M. Oudich, Y. Li, B. Assouar, Acoustic energy harvesting based on a planar acoustic metamaterial, Appl. Phys. Lett. 108 (2016).
- [20] Y. Ming, C. Ziping, L. Jun, et al., Acoustic metastructure for effective low-frequency acoustic energy harvesting, J. Low Freq. Noise Vib. Act. Control 37 (2018) 1015–1029.
- [21] M. Kumar, M. Kumar, Analysis of metamaterials—for its different properties and areas of applications, Int. J. Eng. Res. Technol. 4 (2015) 76–80.
- [22] J.D. Quadros, R. Murikkoli, Y.I. Mogul, M. Mohin, A. Aabid, M. Baig, O.S. Ahmed, Fatigue behaviour of additively manufactured meta-biomaterials for biomedical applications: a review, Results Eng. (2025) 105761.
- [23] N. Gao, Z. Zhang, J. Deng, X. Guo, B. Cheng, H. Hou, Acoustic metamaterials for noise reduction: a review, Adv. Mater. Technol. 7 (2022) 2100698.
- [24] S.A. Cummer, D. Schurig, One path to acoustic cloaking, New J. Phys. 9 (2007) 45.
- [25] B.-I. Popa, L. Zigoneanu, S.A. Cummer, Experimental acoustic ground cloak in air, Phys. Rev. Lett. 106 (2011) 253901.
- [26] A. Climente, D. Torrent, J. Sánchez-Dehesa, Sound focusing by gradient index sonic lenses, Appl. Phys. Lett. 97 (2010).

- [27] J. Zhao, B. Bonello, O. Boyko, Focusing of the lowest-order antisymmetric lamb mode behind a gradient-index acoustic metalens with local resonators, Phys. Rev. B 93 (2016) 174306.
- [28] G. Ma, M. Yang, S. Xiao, Z. Yang, P. Sheng, Acoustic metasurface with hybrid resonances. Nat. Mater. 13 (2014) 873–878.
- [29] V. Romero-García, G. Theocharis, O. Richoux, A. Merkel, V. Tournat, V. Pagneux, Perfect and broadband acoustic absorption by critically coupled sub-wavelength resonators, Sci. Rep. 6 (2016) 19519.
- [30] V. Alamo Vargas, E. Gourdon, A. Ture Savadkoohi, Nonlinear softening and hardening behaviour in Helmholtz resonators for nonlinear regimes, Nonlinear Dyn. 91 (2018) 217-231
- [31] K.A. Omoteso, O. Ozioko, O. Bagdasar, T.O. Roy-Layinde, U.H. Diala, Numerical analyses of acoustic vibrational resonance in a Helmholtz resonator, Nonlinear Dyn. (2024) 1–21.
- [32] J. Lan, Y. Li, H. Yu, B. Li, X. Liu, Nonlinear effects in acoustic metamaterial based on a cylindrical pipe with ordered Helmholtz resonators, Phys. Lett. A 381 (2017) 1111–1117.
- [33] C.M. Donahue, P.W. Anzel, L. Bonanomi, T.A. Keller, C. Daraio, Experimental realization of a nonlinear acoustic lens with a tunable focus, Appl. Phys. Lett. 104 (2014).
- [34] S. Zhang, L. Yin, N. Fang, Focusing ultrasound with an acoustic metamaterial network, Phys. Rev. Lett. 102 (2009) 194301.
- [35] B. Liang, B. Yuan, J.-c. Cheng, Acoustic diode: rectification of acoustic energy flux in one-dimensional systems, Phys. Rev. Lett. 103 (2009) 104301.
- [36] X.-F. Li, X. Ni, L. Feng, M.-H. Lu, C. He, Y.-F. Chen, Tunable unidirectional sound propagation through a sonic-crystal-based acoustic diode, Phys. Rev. Lett. 106 (2011) 084301.
- [37] J.-F. Robillard, K. Muralidharan, J. Bucay, P. Deymier, W. Beck, D. Barker, Phononic metamaterials for thermal management: an atomistic computational study, Chin. J. Phys. 49 (2011) 448–461.
- [38] N. Boechler, G. Theocharis, C. Daraio, Bifurcation-based acoustic switching and rectification, Nat. Mater. 10 (2011) 665–668.
- [39] R. Ramlan, M. Brennan, B. Mace, I. Kovacic, Potential benefits of a non-linear stiffness in an energy harvesting device, Nonlinear Dyn. 59 (2010) 545–558.
- [40] L. Gammaitoni, I. Neri, H. Vocca, Nonlinear oscillators for vibration energy harvesting, Appl. Phys. Lett. 94 (2009) 164102.
- [41] M.G. Tehrani, S.J. Elliott, Extending the dynamic range of an energy harvester using nonlinear damping, J. Sound Vib. 333 (2014) 623–629.
- [42] K. Omoteso, T. Roy-Layinde, U. Diala, Performance boost of an electromagnetic energy harvester using vibrational resonance, Int. J. Non-Linear Mech. (2024) 104989.
- [43] U. Diala, Y. Zhu, R. Gunawardena, Investigative study of the effect of damping and stiffness nonlinearities on an electromagnetic energy harvester at low-frequency excitations, Machines 12 (2024) 30.
- [44] Y. Wang, X. Zhu, T. Zhang, S. Bano, H. Pan, L. Qi, Z. Zhang, Y. Yuan, A renewable low-frequency acoustic energy harvesting noise barrier for high-speed railways using a Helmholtz resonator and a pvdf film, Appl. Energy 230 (2018) 52–61.
- [45] S.R. Anton, H.A. Sodano, A review of power harvesting using piezoelectric materials (2003–2006), Smart Mater. Struct. 16 (2007) R1.
- [46] M. Yuan, Z. Cao, J. Luo, Z. Pang, Helix structure for low frequency acoustic energy harvesting, Rev. Sci. Instrum. 89 (2018).
- [47] M. Yuan, Z. Cao, J. Luo, J. Zhang, C. Chang, An efficient low-frequency acoustic energy harvester, Sens. Actuators A, Phys. 264 (2017) 84–89.
- [48] S.B. Horowitz, M. Sheplak, L. Cattafesta, T. Nishida, A mems acoustic energy harvester, J. Micromech. Microeng. 16 (2006) S174.
- [49] F. Liu, A. Phipps, S. Horowitz, L. Cattafesta, T. Nishida, M. Sheplak, Acoustic energy harvesting using an electromechanical Helmholtz resonator, J. Acoust. Soc. Am. 125 (2009) 2596.
- [50] X. Peng, Y. Wen, P. Li, A. Yang, X. Bai, Enhanced acoustoelectric coupling in acoustic energy harvester using dual Helmholtz resonators, IEEE Trans. Ultrason. Ferroelectr. Freq. Control 60 (2013) 2121–2128.
- [51] X. Peng, Y. Wen, P. Li, A. Yang, X. Bai, A wideband acoustic energy harvester using a three degree-of-freedom architecture, Appl. Phys. Lett. 103 (2013).
- [52] S.-H. Kim, C.-H. Ji, P. Galle, F. Herrault, X. Wu, J.-H. Lee, C.-A. Choi, M.G. Allen, An electromagnetic energy scavenger from direct airflow, J. Micromech. Microeng. 19 (2009) 094010.
- [53] S. Noh, H. Lee, B. Choi, A study on the acoustic energy harvesting with Helmholtz resonator and piezoelectric cantilevers, Int. J. Prec. Eng. Manuf. 14 (2013) 1629–1635.

- [54] D. Li, M. Hu, F. Wu, K. Liu, M. Gao, Z. Ju, J. Zhao, A. Bao, Design of tunable low-frequency acoustic energy harvesting barrier for subway tunnel based on an optimized Helmholtz resonator and a pzt circular plate, Energy Rep. 8 (2022) 8108–8123
- [55] K. Ma, T. Tan, Z. Yan, F. Liu, W.-H. Liao, W. Zhang, Metamaterial and Helmholtz coupled resonator for high-density acoustic energy harvesting, Nano Energy 82 (2021) 105693.
- [56] G.-S. Liu, Y.-Y. Peng, M.-H. Liu, X.-Y. Zou, J.-C. Cheng, Broadband acoustic energy harvesting metasurface with coupled Helmholtz resonators, Appl. Phys. Lett. 113 (2018).
- [57] A. Yang, P. Li, Y. Wen, C. Lu, X. Peng, J. Zhang, W. He, Enhanced acoustic energy harvesting using coupled resonance structure of sonic crystal and Helmholtz resonator, Appl. Phys. Express 6 (2013) 127101.
- [58] P. Fan, S. Wang, X. Wang, A high-performance conical-neck Helmholtz resonatorbased piezoelectric self-powered system for urban transportation, Appl. Acoust. 220 (2024) 109945.
- [59] B. Li, H. Chen, B. Xia, L. Yao, Acoustic energy harvesting based on topological states of multi-resonant phononic crystals, Appl. Energy 341 (2023) 121142.
- [60] R. Wada, H. Takahashi, Frequency-specific highly sensitive acoustic sensor using a piezoresistive cantilever element and parallel Helmholtz resonators, Sens. Actuators A. Phys. 345 (2022) 113808.
- [61] T. Li, Z. Wang, H. Xiao, Z. Yan, C. Yang, T. Tan, Dual-band piezoelectric acoustic energy harvesting by structural and local resonances of Helmholtz metamaterial, Nano Energy 90 (2021) 106523.
- [62] A.F. Vakakis, Inducing passive nonlinear energy sinks in vibrating systems, J. Vib. Acoust. 123 (2001) 324–332.
- [63] S. Rajasekar, M.A.F. Sanjuán, Nonlinear Resonances, Springer Series in Synergetics, Springer, Switzerland, 2016.
- [64] L.E. Kinsler, A.R. Frey, A.B. Coppens, J.V. Sanders, Fundamentals of Acoustics, John Wiley and Sons, 2000.
- [65] M. Kovaláakov, M. Kladivová, Z. Gibová, Helmholtz resonator in laboratory experiments, Phys. Teach. 58 (2020) 179–181.
- [66] T.S. Amer, R. Starosta, A. Almahalawy, A.S. Elameer, The stability analysis of a vibrating auto-parametric dynamical system near resonance, Appl. Sci. 12 (2022) 1737
- [67] T.S. Amer, R. Starosta, A.S. Elameer, M.A. Bek, Analyzing the stability for the motion of an unstretched double pendulum near resonance, Appl. Sci. 11 (2021) 9520.
- [68] Z. Liu, J. Zhan, M. Fard, J.L. Davy, Acoustic properties of a porous polycarbonate material produced by additive manufacturing. Mater. Lett. 181 (2016) 296–299.
- [69] G. Fusaro, L. Barbaresi, M. Cingolani, M. Garai, E. Ida, A. Prato, A. Schiavi, Investigation of the impact of additive manufacturing techniques on the acoustic performance of a coiled-up resonator, J. Acoust. Soc. Am. 153 (2023) 2921.
- [70] L. Suárez, M. del Mar Espinosa, Assessment on the use of additive manufacturing technologies for acoustic applications, Int. J. Adv. Manuf. Technol. 109 (2020) 2691–2705
- [71] A. Ciochon, J. Kennedy, R. Leiba, L. Flanagan, M. Culleton, The impact of surface roughness on an additively manufactured acoustic material: an experimental and numerical investigation, J. Sound Vib. 546 (2023) 117434.
- [72] L. Li, Y. Liu, F. Zhang, Z. Sun, Several explanations on the theoretical formula of Helmholtz resonator, Adv. Eng. Softw. 114 (2017) 361–371.
- [73] B. Maamer, A. Boughamoura, A.M.F. El-Bab, L.A. Francis, F. Tounsi, A review on design improvements and techniques for mechanical energy harvesting using piezoelectric and electromagnetic schemes, Energy Convers. Manag. 199 (2019) 111973.
- [74] H. Li, C. Tian, Z.D. Deng, Energy harvesting from low frequency applications using piezoelectric materials, Appl. Phys. Rev. 1 (2014).
- [75] C. Gu, Y. Chen, W. Chen, P. Zhao, Acoustic Energy Harvester by Electromagnetic Mechanisms and Helmholtz Resonator, IOP Conference Series: Earth and Environmental Science, vol. 617, IOP Publishing, 2020, p. 012038.
- [76] A. Mukherjee, G. Agnivo, Determination of Natural Frequency of Euler's Beams Using Analytical and Finite Element Method, Department of Mechanical Engineering, 2010
- [77] J. Liang, W.-H. Liao, Impedance modeling and analysis for piezoelectric energy harvesting systems, IEEE/ASME Trans. Mechatron. 17 (2011) 1145–1157.
- [78] D. Yu, Q. Tao, Q. Liu, Y. Jin, Y. Sun, P. Fu, Lifecycle management of urban renewal enabled by Internet of things: development, application, and challenges, Results Eng. (2025) 105706.
- [79] M. Brennan, I. Kovacic, A. Carrella, T. Waters, On the jump-up and jump-down frequencies of the Duffing oscillator, J. Sound Vib. 318 (2008) 1250–1261.